AN ABSTRACT OF THE THESIS OF

Richard Wesley Strayer for the degree of Ph.D.
(Name of Student) (Degree)

in Physics presented on December 11, 1973
(Major department) (Date)

Title: WORK FUNCTION MEASUREMENTS OF SINGLE CRYSTAL SURFACES BY THE FIELD EMISSION RETARDING POTENTIAL METHOD

Redacted for privacy

Abstract approved: _____
(Signature)
Dr. James J. Brady

Using the field emission retarding potential method true work functions have been measured for several monocrystalline substrates; the values obtained are the following:

W(110)	5.25 ± 0.02 eV
W(100)	4.63 ± 0.02
W(111)	4.47 ± 0.02
Ir(111)	5.76 ± 0.04
Ir(110)	5.42 ± 0.02
Nb(100)	4.18 ± 0.02
Ni(100)	5.53 ± 0.05
Cu(100)	5.10 ± 0.05

The electron elastic and inelastic reflection coefficients from several of these surfaces have also been examined near zero primary beam energy.

Work Function Measurements of Single Crystal Surfaces by the Field Emission Retarding Potential Method

by

Richard Wesley Strayer

A THESIS

submitted to

Oregon State University

in partial fulfillment of
the requirements for the
degree of

Doctor of Philosophy

Commencement June 1974

APPROVED:

Redacted for privacy

Professor of Department of Physics
in charge of major

Redacted for privacy

Head of Department of Physics

Redacted for privacy

Dean of Graduate School

Date thesis is presented December 11, 1973

Typed by Marsha Mackie for Richard Wesley Strayer

ACKNOWLEDGEMENTS

I wish to express my sincere appreciation to Dr. James J. Brady, my major professor, for his encouragement and advice during the course of this thesis project. I also wish to thank Dr. Larry Schecter for his assistance. In addition, I wish to thank Dr. Lynwood W. Swanson for his advice and direction of the project under which this work was performed, Mr. William A. Mackie for his assistance in acquisition and computer analysis of the data, and Mr. Noel Martin, Mr. Howard Benson and Mr. Richard Rathkey for their very fine work in the construction of the experimental tube. Finally I would like to thank Field Emission Corporation and Linfield Research Institute, both of McMinnville, Oregon, for the use of their facilities during the course of this work, and the Electric Power Group at Lewis Research Center, National Aeronautics and Space Administration, Cleveland, Ohio, for their continuing interest and financial support for this project.

TABLE OF CONTENTS

LIST OF FIGURES

LIST OF TABLES

WORK FUNCTION MEASUREMENTS OF SINGLE CRYSTAL BY THE FIELD EMISSION RETARDING POTENTIAL METHOD

I. INTRODUCTION

A. Definition of Work Function

The term "work function" was apparently first used in its present meaning by H.H. Lester in 1916, when he wrote: "the work done by an escaping electron is represented in the well-known Richardson equation $I = a\theta^{1/2}\exp(-b/\theta)$ by the constant b. In order to justify completely the assumption involved in b, such a work function should be found to exist and its magnitude should be identical to b" (1). The concept of the work function had already been implicit for several years in the writings of Richardson, Langmuir and others, but it is more difficult to date the inception of the concept than that of the name.

The work function ϕ of a uniform metal surface is defined (2,3) as the difference between the electrochemical potential $\bar{\mu}$ of the electrons within the bulk metal relative to the mean electrostatic potential of the interior and the change in electrostatic potential $\Delta\Phi$ across the metal surface (Figure 1):

$$\phi = \Delta\Phi - \bar{\mu}. \qquad (1)$$

Thus ϕ is equal to the minimum work necessary to remove an electron from the Fermi energy level of the metal at $0^{\circ}K$ and in the absence of applied electric fields. The term $\Delta\Phi$ may be thought of as arising from a double layer of electric charge at the surface; thus any change in the equilibrium of the surface double layer is reflected in a change in the work function. The term $\bar{\mu}$ is a volume property independent of the structure of the surface; for this reason it is sometimes called the "inner work function."

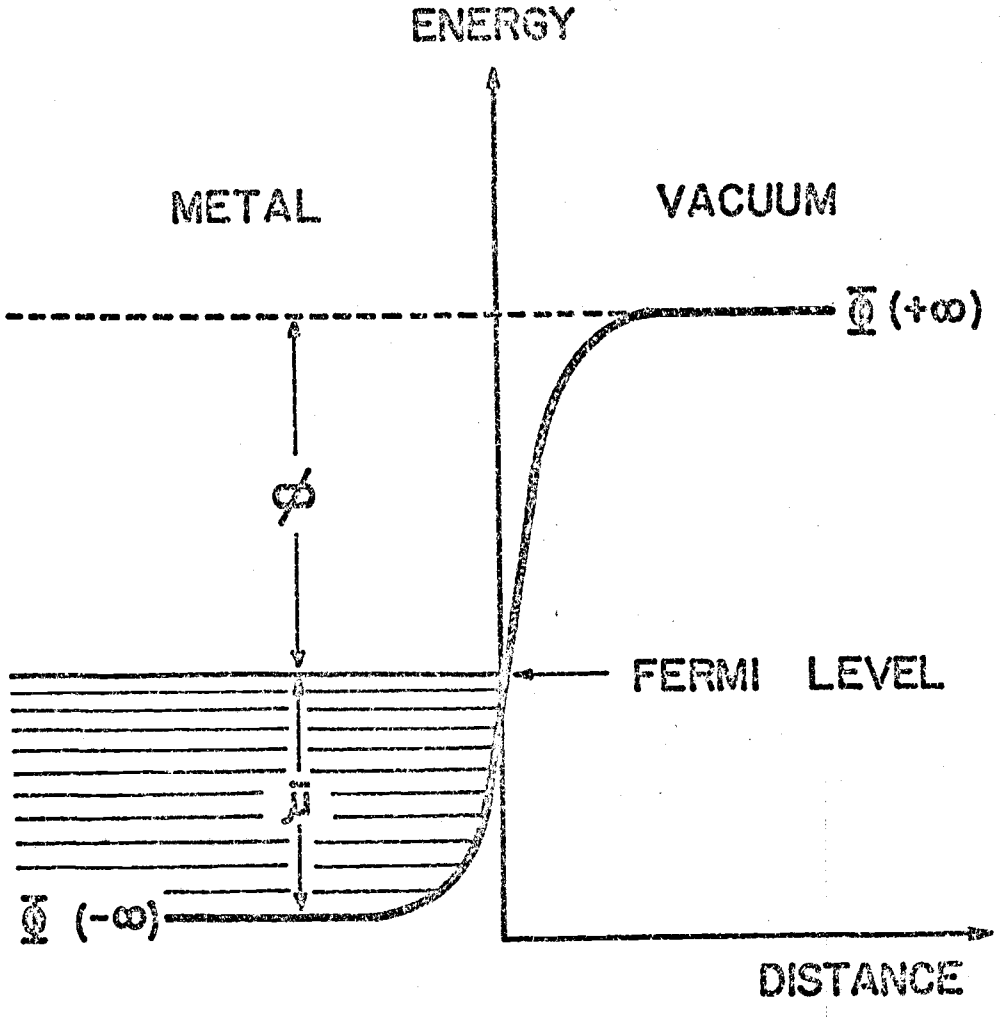

Figure 1. Schematic representation of various energies relevant to the definition of work function

B. Importance

Interest in the work function is derived from these main areas: (1) the technology of electron-emission devices, (2) the experimental study of surfaces and (3) the electronic theories of metals and metal interfaces.

Early research on the work function was motivated in part by the need for efficient and stable electron sources, especially in the newly developing vacuum tube industry. This need has continued into the present with the development of direct conversion thermionic devices, with increasingly stringent cathode requirements for both transmission and scanning electron microscopes, for the improvement in performance of radiation detectors, among many others. The continuing search for electron sources capable of operating under adverse environmental conditions requires a more fundamental understanding of those parameters affecting the work function.

In the study of surfaces, measurement of the work function provides a relatively simple method of monitoring the state of the surface, since any change in surface conditions reflected in a disturbance of the surface double layer affects the work function. Thus such processes as adsorption, diffusion and desorption of an adsorbed species may be monitored by the change in work function due to the dipole moment of the species on the surface. Likewise changes in surface structure resulting in the appearance or disappearance of crystal planes making up the surface are reflected in changes in the variation of the work function over the surface. In many surface studies, knowledge of the work function of the clean metal surface is a necessary starting point.

In recent years considerable progress has been made in the application of electron theories of metals to the electronic structure of clean metal surfaces (4). One feature of these surface theories is the

calculation of the work function; thus comparison of calculated work function values with experimental values is one criterion by which metal surface theories may be evaluated. For this, accurate experimental values of the work function are needed for a large number of single crystal metal surfaces.

C. Methods of Work Function Measurement

Due to the above motivations, an increasing number of measurements of clean, single crystal face work function have been reported. Primarily due to the perennial problem of surface purity and partly due to inadequacies in the theoretical description of the various modes of electron emission one finds an inordinate amount of disagreement in the literature values of work function (5,6). However, the rapid advance in the methodology of fabricating ultra pure metals along with the increasing number of ways of cleaning and sensitively detecting minute concentrations of surface impurities is gradually eliminating surface contamination as a major factor in arriving at a consensus as to the appropriate clean single crystal face work function values. A further problem of lesser importance is that of maintaining desired crystallographic orientation at the surface during the cleaning procedure; this problem can be detected by LEED (low energy electron diffraction) and Laue X-ray analysis and occurs for relatively few materials.

It has become increasingly obvious that there can be significant differences in the values of work function for the same material and crystallographic direction depending upon the measuring technique used. In particular, for certain planes of some metals, work function values determined by field emission techniques are several tenths of an electron volt higher than values determined in other ways. For example, the field emission value of the work function for the

(110) plane of tungsten is at least 0.6 eV higher than that obtained by other methods (7). These large differences in experimental values of work function for the same metal suggest examination of the theoretical models upon which work function measuring techniques are based.

Work function measuring techniques may be divided into four main classes: (1) electron emission methods, (2) contact potential difference methods, (3) surface ionization methods, and (4) retarding potential methods. Contact potential difference methods only measure the work function of one surface relative to the work function of a second surface and thus do not provide values of the absolute (or true) work function that is of interest here. Surface ionization methods determine the work function at elevated temperatures with the aid of simplifying assumptions concerning statistical weights and reflection coefficients of the various species involved; thus it is hard to relate the measured values to the work function as defined above (6).

The primary electron emission processes whereby work function values of the emitter can be theoretically obtained are thermionic, photoelectric and field emission. The assumptions, limitations and applicability of each of these methods for obtaining work function values have been adequately described in the literature (see, for example, Rivière, 1969 (6)). The basic theoretical model utilized for description of these electron emission processes is the Sommerfeld (8,9) free electron model, which is severely strained in its application to a wide variety of non-free electron refractory metal emitters. This limitation has been described for thermionic, field and photo emission by Itskovich (10). Recent field emission energy distribution measurements have given dramatic experimental evidence as to the inability of the Sommerfeld based Fowler-Nordheim theory (11,12) to explain the results from all crystallographic directions of tungsten,

molybdenum and copper emitters (7,13,14). Besides the fundamental problem of model applicability, a host of minor complex effects such as the temperature dependence of the work function, variable coefficients and the Schottky effect must be carefully incorporated into the theoretical framework of the emission process.

Retarding potential methods of measuring work function circumvent most of the difficulties associated with the emission methods by determining the work function of an electron collector surface. However, there are only two methods, an experimentally complex adaptation of the Shelton (15) thermionic electron method and the field electron retarding potential (FERP) method by which the non-relative work function of an electron collector surface can be measured. As will be shown in Chapter II, the success of the FERP method rests on the theoretical and experimentally verifiable fact that the voltage threshold for collection of field emitted electrons occurs at the Fermi level E_f at 0^oK or can be described by a Boltzmann tail, i.e., $\exp(E_f - E)/kT$, at temperature T. The several experimental studies of the total energy distribution (TED) now in the literature (7,16,17) provide a firm basis for the validity of the preceding fact; also if the appropriate crystallographic direction of a refractory metal emitter is employed, the free electron based Fowler-Nordheim model of field emission is adequate for this application.

D. Background

Henderson and Badgley (18) first used the retarding potential method as a way of investigating the energy distribution of field emitted electrons; they found that a voltage greater than 4.3 V had to be applied to a copper collector in order to collect a measurable portion of the field emitted electrons. Dyke (19) originally recognized the significance of the field emission retarding potential technique for allowing the work function of the collector to be measured

without requiring any knowledge of the work function of the emitter. He used the technique to determine the work function of polycrystalline metal surfaces; recently, Holscher (20) revived the technique to measure the work functions of freshly evaporated gold and nickel films under ultra-high vacuum conditions. In this work the field emission retarding potential technique is employed to obtain the work function of selected crystal faces of macroscopic single crystal metal targets.

II. THEORETICAL CONSIDERATIONS

A. Basis of the Technique

The potential energy diagram of Figure 2 illustrates the essential features of the field emission retarding potential method. A high electrostatic field applied to an emitter surface narrows the surface potential barrier, so that electrons occupying energy levels near the Fermi level can tunnel through the barrier. The emitter electrons are accelerated in the region between the emitter and the anode, but are then retarded in the region between the anode and the collector. If the collector is connected electrically to the emitter, the Fermi levels of the two metals are at the same level and the emitted electrons are stopped by a potential barrier at the collector surface equal to its work function ϕ_c. To collect the field emitted electrons, a voltage V_c with magnitude (with respect to the emitter) $V_c \geq \phi_c$ must be applied to the collector. Thus, as shown in Figure 2, at 0°K the onset of current at the collector occurs when $V_c = \phi_c$, the collector work function.

The shape of the collector current-voltage curve $I_c(V_c)$ is determined primarily by the energy distribution of the emitted electrons; theoretically, this distribution is given by assuming the Sommerfeld (8,9) free electron model for the electron distribution among the energy levels within the metal (7,21):

$$dI_c/d\epsilon = I_o e^{\epsilon/d} / [d(1 + e^{\epsilon/kT})] \qquad (2)$$

where dI_c is the differential field emitted current between energy ϵ and $\epsilon + d\epsilon$ (where ϵ is the energy of an electron relative to the Fermi level, $\epsilon = E - E_f$), T is the emitter temperature, and the value of d is given by

$$d = \hbar eF/2(2m\phi_e)^{1/2} t(y) = 0.976F/\phi_e^{1/2} t(y) \text{ (eV)}, \qquad (3)$$

where the electric field F and the emitter work function ϕ_e are in

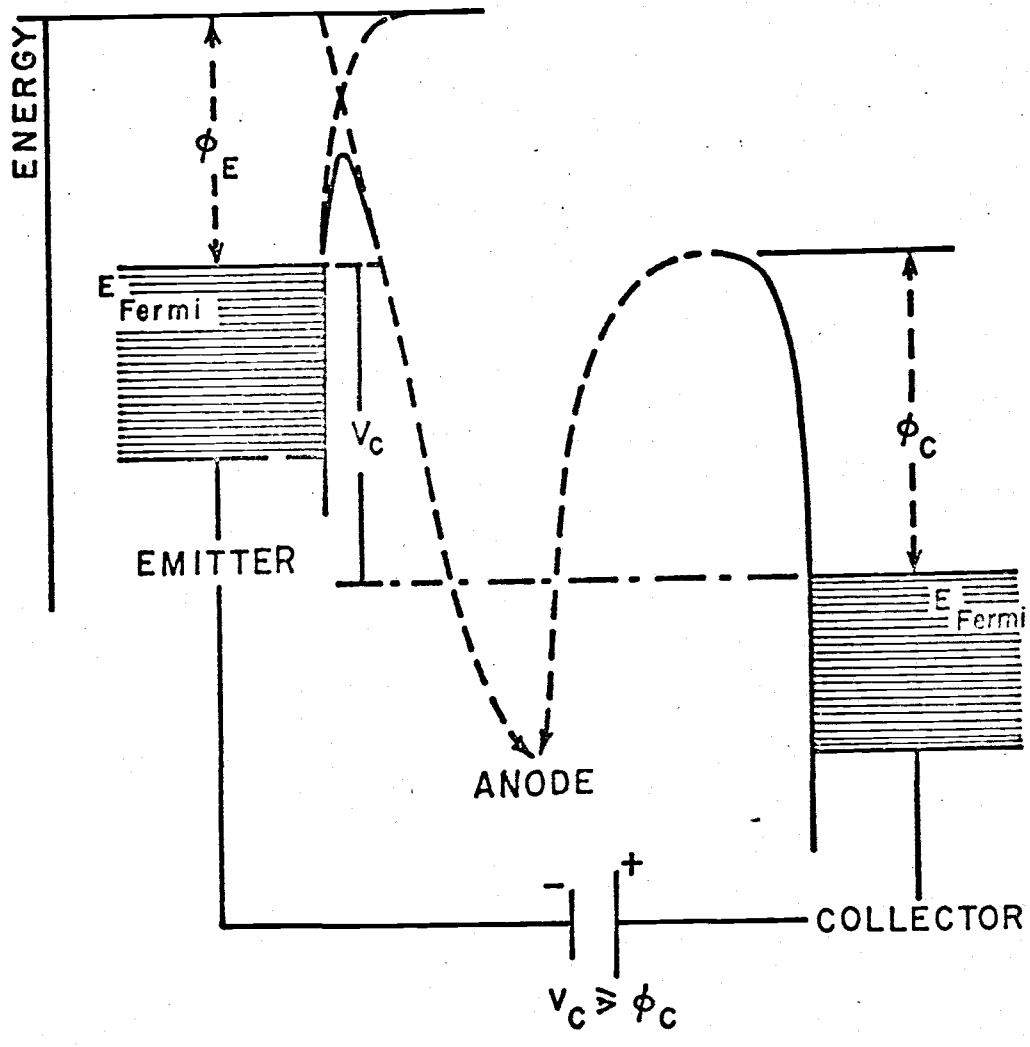

Figure 2. Potential energy diagram for a field electron retarding potential analyzer. When the collector is biased such that only electrons from the Fermi level of the emitter can reach the collector, the battery voltage V_C is equal to the collector work function ϕ_C

$V/\mathring{A}$ and eV, respectively. The maximum emitter current I_o in Equation (2) is given by the well-known Fowler-Nordheim equation (10,11)

$$I_o = \frac{e^3F^2A_o}{8\pi h\phi_e t^2(y)} \exp\left[-4(2m\phi_e^3)^{1/2}v(y)/3heF\right]$$
$$= \frac{1.5\times10^{10}}{\phi_e t^2(y)} F^2A_o \exp\left[-0.683\phi_e^{3/2}v(y)/F\right] \text{ (A)}, \quad (4)$$

where A_o is the area of the emitting surface from which the collected current originates. The image correction terms t(y) and v(y) are slowly varying tabulated functions of the auxiliary variable $y = (e^3F)^{1/2}/\phi_e$ (22).

From Equation (2), it is apparent that $dI_c/d\epsilon$ turns on abruptly at the emitter Fermi level when T is small and decays exponentially with decreasing electron energy. The value of the half width Δ of the total energy distribution can be obtained from Equation (2) so that at $T = 0^oK$, Δ is given by

$$\Delta = 0.69d. \quad (5)$$

Since the practical value of d varies from 0.1 to 0.3 eV, the experimental half widths fall in the range from 0.07 to 0.2 eV.

For the retarding potential method, the emitted electrons can be collected at a metal surface of work function ϕ_c only if their total energy meets the condition

$$E > \phi_c + E_f - V_c \quad (6)$$

where V_c is the emitter-to-collector bias potential; thus, decreasing V_c allows all electrons down to the energy level $\epsilon = \phi_c - V_c$ to be collected at 0^oK. The condition $V_c = \phi_c$ represents the current cut-off since electronic states above E_f are not populated, and the total collected current I_c at a specified value of ϵ is given by

$$I_c = \frac{I_o}{d} \int_{\epsilon}^{o} e^{\epsilon/d} d\epsilon = I_o(1 - e^{\epsilon/d})$$
$$= I_o \left[1 - e^{-(V_c - \phi_c)/d}\right] . \qquad (7)$$

Equation (7) is plotted as a solid curve in Figure 3 along with experimental data for W(110) surface.

B. Deviations from the Theoretical Collector Curve

Experimental collector current-voltage curve differs from the theoretical curve (Equation 7) due to several effects. At emitter temperatures above 0°K there is a deviation in I_c from the ideal cut-off at $V_c = \phi_c$, because there are electrons emitted from energy levels above the Fermi level. The effect of temperature on the total energy distribution of field emitted electrons has been calculated theoretically (7,21) and verified experimentally (7,16). Increasing temperature broadens the energy distribution and lowers its peak value (Figure 1 of reference 7). At low temperatures the deviation from the ideal cut-off is small and may be easily corrected for.

If the assumption of a free electron density of states within the emitter is not valid, there can be modifications of Equation (7) due to band structure and energy exchange effects such as electron-hole and electron-phonon interactions (23). Experimentally measured variations in electron energy distribution curves for the <100> directions of tungsten and molybdenum have been correlated with certain features of energy-surface shapes inferred from bulk electronic measurements (7,13). Changes in Equation (7) due to band structure effects can be avoided by choosing an emission direction for which the corresponding energy distribution curve is "normal", i.e., exhibits the exponential behavior of Equation (2).

The finite resolution of the energy analyzing system may modify the collector current-voltage curve. Young and Kuyatt (24) have cal-

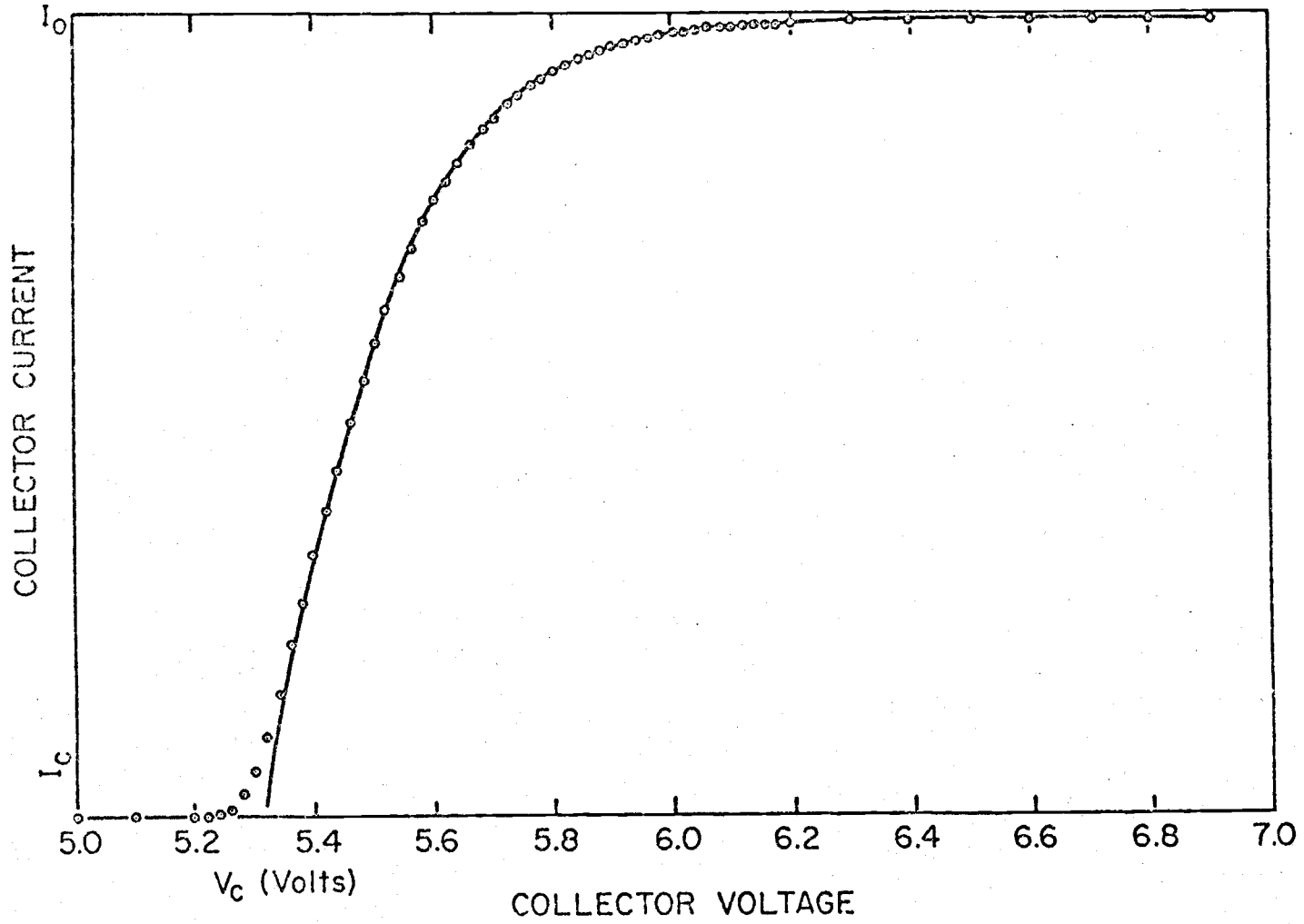

Figure 3. Collector current I_c as a function of collector voltage V_c for the W(110) surface. The solid curve is the theoretical curve for 0°K (Equation 7)

culated the influence of energy analyzer transmission function upon field emission energy distributions, and have found in general that increasing energy analyzer width broadens the energy distribution and lowers its peak value in much the same manner as increasing temperature. Furthermore, they have found that the slope of the log of the energy distribution is changed by less than 1% when the analyzer width is changed from 0 to 100 meV; in terms of the collector current-voltage curve, this means the energy analyzer width affects mainly the region of the cut-off, but not the upper portion of the $I_c(V_c)$ curve, which still may be used to determine ϕ_c.

Other effects that can modify the collector current-voltage curve are those due to the properties of the collector itself, such as its perpendicularity to the electron beam, its surface roughness, its heterogeniety in work function, and its reflection coefficient (this latter to be discussed in section D). The loss in resolution ΔE due to an electron beam of energy E striking a target at an angle θ is given by (25)

$$\Delta E = E \sin^2 \theta. \tag{8}$$

For 1 eV electrons the change in resolution for an angle of 1.5 degrees is less than 1 meV, and thus negligible. As pointed out by Holscher (20), the effect of irregularities in the equipotential lines near the collector, caused by collector surface roughness, can be minimized by reducing the potential drop in the region near the collector. According to Heil (26), the different potentials presented at the surface of a metal by the differently oriented crystal surfaces converge exponentially to the average potential as one moves away from the surface. Therefore, when the potential drop in the region of the collector is kept small, the measured work function for the collector will be an area average of the differing work functions on the collector surface.

C. Methods of Obtaining Work Function from Experimental Data

By rewriting Equation (7) in the working form

$$\log_{10} \Delta I_c/I_o = \phi_c/2.3\,d - V_c/2.3\,d, \tag{9}$$

where $\Delta I_c = I_o - I_c$, it is clear that the values of ϕ_c and d can be obtained from the intercept and slope respectively of a plot of $\log_{10} \Delta I_c/I_o$ versus V_c, such as shown in Figure 4. At emitter temperatures above 0^oK, $\log_{10} \Delta I_c/I_o$ versus V_c deviates from linearity due to the Boltzmann distribution of electrons in states above E_f. The theoretically expected effect of temperature on the TED has been verified experimentally and is of little consequence to the accuracy of utilizing Equation (9) to obtain ϕ_c at $T \leq 300^oK$ (24). This can be verified by noting that the temperature accounts for only a small deviation from linearity in the $\log_{10} \Delta I_c/I_o$ versus V_c plot near $V_c = \phi_c$ as shown in Figure 4.

Alternatively, one may obtain ϕ_c by noting that the value of V_c at $I_c/I_o = 0.5$ when inserted into Equation (9) yields

$$\phi_c = V_c(1/2) - d \ln 2 \tag{10}$$

where $V_c(1/2)$ is the value of V_c for which $I_c/I_o = 0.5$. Equation (10) is strictly applicable only for $T = 0^oK$; however, the temperature correction to $V_c(1/2)$ is minor and only amounts to ~ 10 meV at 300^oK. The principal source of experimental error in both of these methods stems from the uncertainty in the experimental values of d and I_o due to electron reflection. This is discussed in greater detail in the next section.

Equation (7) may be differentiated with respect to ϵ in order to obtain the difference in energy ϵ_p between the peak of the TED and the Fermi energy level:

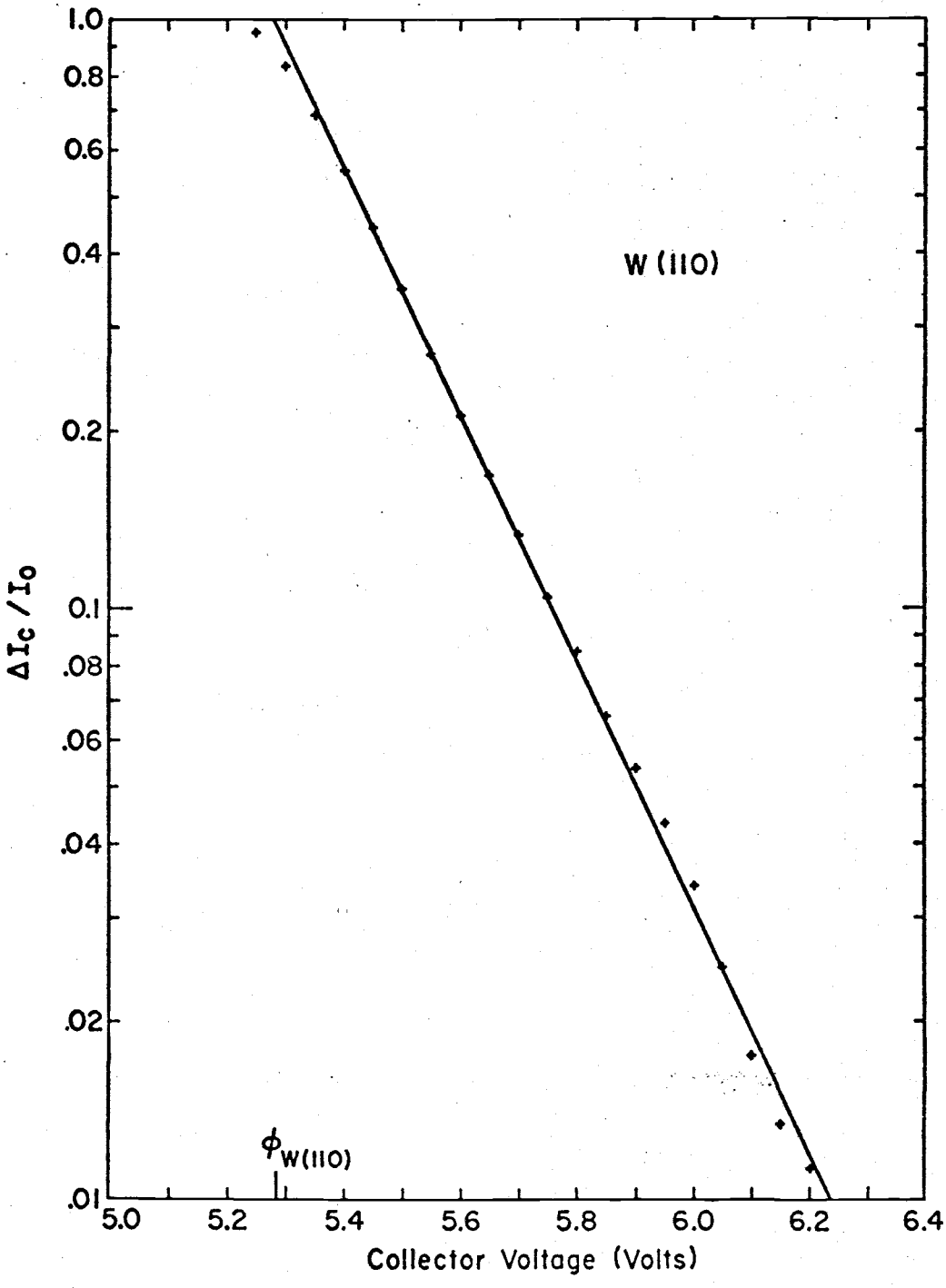

Figure 4. Plot of $\log_{10} \Delta I/I_o$ versus collector voltage for the W(110) surface. The intercept of the abscissa at $\Delta I/I_o = 1$ gives ϕ_c according to Equation (9).

$$\epsilon_p = kT \ln \frac{kT}{d - kT}. \qquad (11)$$

This equation, plotted in Figure 5 at several values of d, may be used to obtain the theoretical value of ϵ_p which is equal to $\phi_c - V_p$. Since V_p (the position of maximum dI_c/dV_c on the energy axis) can be obtained experimentally, the value of ϕ_c can be obtained directly from the TED curve and Figure 5. Since in practice ϵ_p is approximately 30 meV, this method gives ϕ_c easily within 1% accuracy.

Even though the assumptions of the Sommerfeld free electron model, upon which Equation (2) and the subsequent equations are based has recently been found to be inadequate for certain crystallographic directions of tungsten (7) and molybdenum (13), the occurrence of the emission threshold at E_f was unchanged for clean emitters. In any case, inadequacies in Equation (2) due to band structure can be easily avoided for this application by choosing an emission direction (e.g., the <111> or <310> of tungsten) for which the corresponding experimental TED curve (7) agrees well with Equation (2). For that reason, oriented field emitters with these directions along the emission axis have been utilized for this study. Thus, all that must be known concerning the emitter in order to apply the FERP method of work function determination is the value of d which can be either calculated with sufficient accuracy from the I(V) characteristics of the emitter using Equation (3) or determined experimentally from Equation (9).

D. Electron Reflection

The one property of the collector that can detract from the complete applicability of the above equations in evaluating ϕ_c is electron reflection near the threshold of collection; reflection cannot be eliminated by the FERP method should it occur. We can indicate the

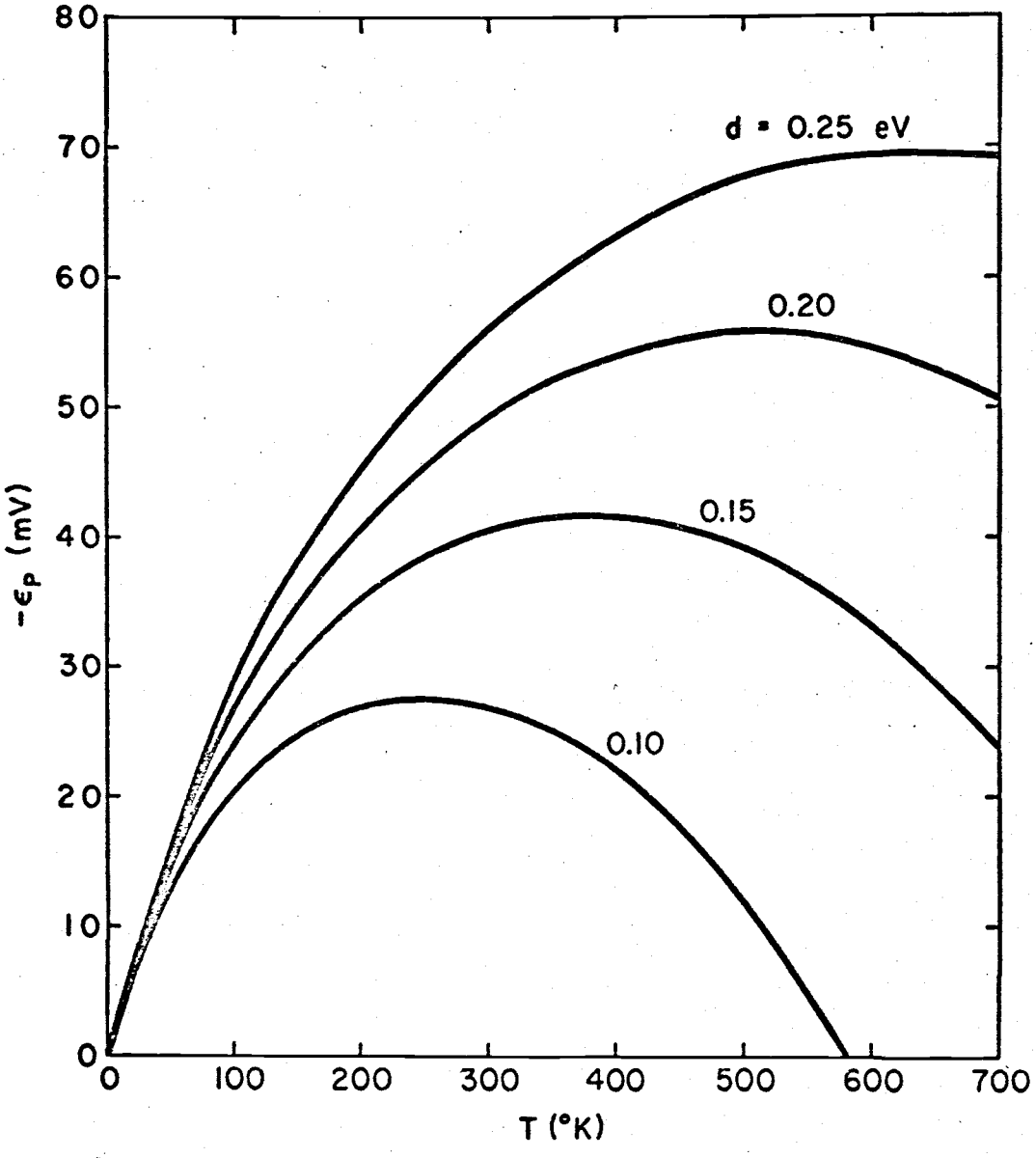

Figure 5. The difference ε_p in energy between the peak of the TED curve and the Fermi level as a function of T and energy parameter d.

effect of reflection on Equation (2) by noting that $I_c = I_p(1 - R)$, where I_p is the primary beam current impinging on the collector, and by defining the energy dependent reflection coefficient $R(\epsilon)$ as $R(\epsilon) = I_r/I_p$, where I_r is the reflected current. With these definitions one may readily show that the experimentally measured quantity $dI_c/d\epsilon$ is given by

$$dI_c/d\epsilon = \alpha(\epsilon)\, dI_p/d\epsilon - I_p d\alpha/d\epsilon, \tag{12}$$

where $\alpha(\epsilon) = 1 - R(\epsilon)$ is the electron acceptance coefficient and $\epsilon = |\phi_c - V_c|$ is the maximum kinetic energy of the collected electrons. Near the collection current threshold (i.e., $\epsilon \sim 0$) the last term of Equation (12) will be small compared to the first since $I_p \to 0$ as $\epsilon \to 0$ and $d\alpha/d\epsilon$ is normally small at $\epsilon = 0$.

However, as the energy of the primary electron beam increases above the threshold voltage considerable change may occur in $\alpha(\epsilon)$ (i.e., $d\alpha/d\epsilon$ becomes large) which in turn will cause serious deviation in the apparent value of I_p. Thus, plotting the data according to Equation (9) in order to obtain an accurate value of ϕ_c and d will not be possible. In like manner it will be difficult to utilize Equation (10) in order to obtain ϕ_c due to the inability to obtain an accurate value of I_o.

In contrast, Equation (11) is basically unaffected by reflection since the last term of Equation (12) can usually be neglected at $\epsilon \simeq \epsilon_p$. We should also point out that a cursory examination of Figure 5 reveals that ϵ_p is very small (less than 40 meV) at practical values of d and T so that uncertainties in the exact position of ϵ_p due to reflection (which will be $<<$ 40 meV) will not introduce appreciable error in the value of ϕ_c. Thus, in the event that detectable reflection should occur for a particular collector at threshold, the evaluation of ϕ_c should be accomplished from the TED curve through Equation (11).

III. APPARATUS

A. Experimental Tube

The experimental tube is diagrammed in Figure 6 and shown in Figure 7. Full dimensions are given in Appendix I. The main features of the tube are the electron optical system, the field emission source and the collector target, each of which is described below.

1. Electron Optical System

The basic requirement of the electron optical system for this application is to transform the highly divergent electron beam into a co-linear beam normal to the collector substrate surface and to simultaneously decelerate it to zero volts. In order to maximize the analyzer energy resolution, the electron source must be highly apertured (26), which in turn causes a very low beam transmission coefficient of the order of 10^{-3} to 10^{-4}. However, if the emitter is to be operated at room temperature the resolution of the analyzer need only be 100 meV (24); therefore, an electron optical system which sacrificed unnecessary resolution was designed for this application in order to obtain a larger collector current to speed data acquisition. Rather than restrict the primary beam to the usual 1^{o} half angle in order to maximize resolution, for this application a half angle of approximately 8^{o} was chosen; depending on the orientation of the emitter this aperture angle allowed a beam transmission of the order of 10%. Currents in the 10^{-7} A range were easily obtained in the focused spot thereby allowing the gun to be used as an electron source for other applications as well.

The electrostatic focusing system used in the analyzer shown in Figure 6 consists of anode, two Einzel lenses and a 200 line/cm decelerating mesh electrode which established parallel equipotential surfaces in front of the collector. All electrodes were made from

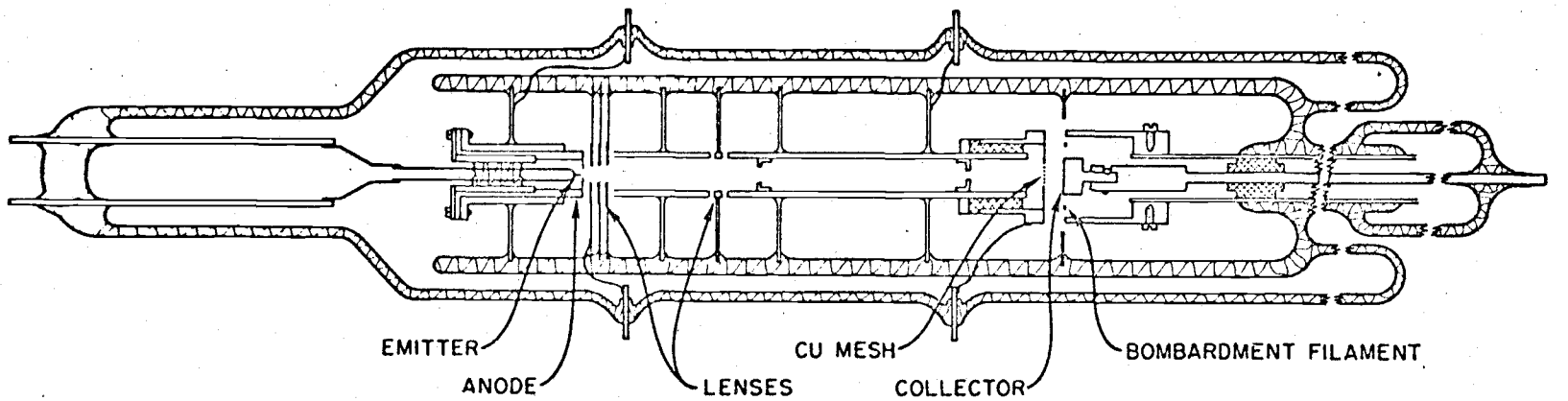

Figure 6. Diagram of FERP tube, showing pertinent features of the electron optical system and the single crystal collector.

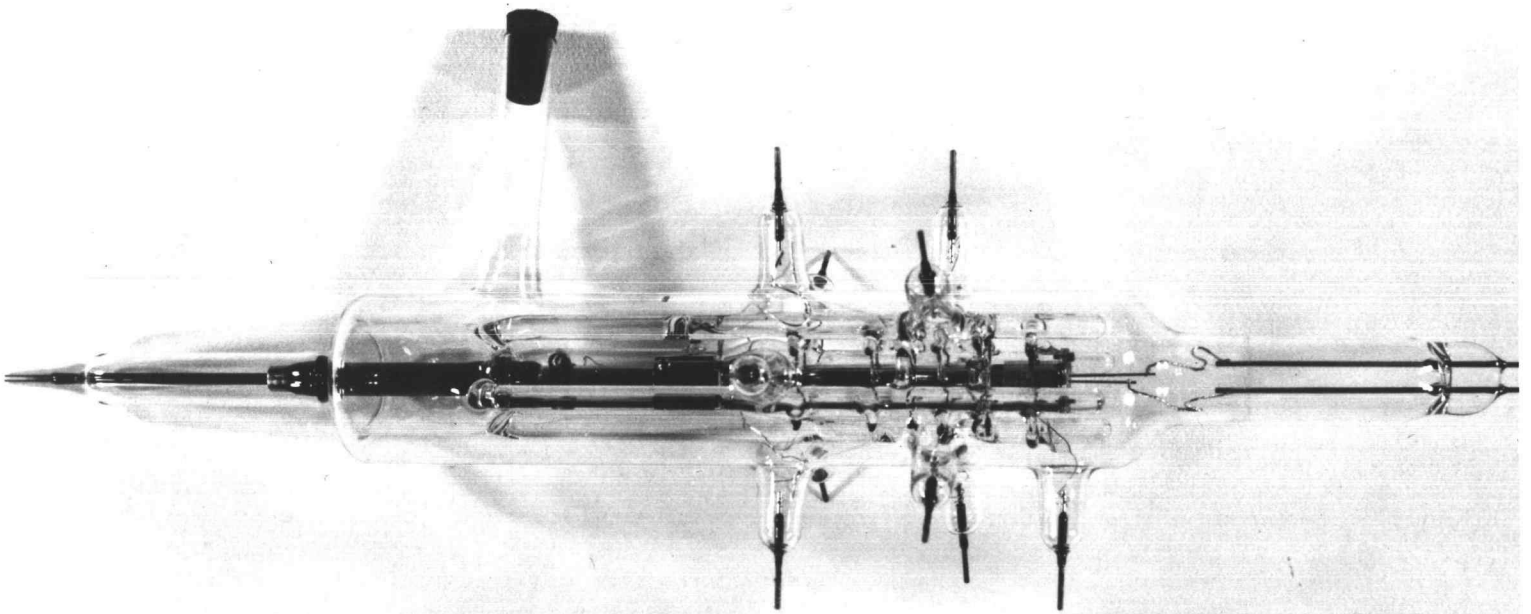

Figure 7. Photograph of the FERP tube.

molybdenum. A two stage electrostatic focusing system with a virtual cross-over in front of the first lens was chosen over a single stage because of its greater optical efficiency. The lens circuitry is shown in Figure 8, and the lens operating voltages given in Table I were arrived at by computer analysis and confirmed experimentally.

TABLE I. OPERATING VOLTAGES ON LENS ELEMENTS (SEE FIGURE 8 WITH EMITTER AT 0 V).

Lens Element	Operating Voltage
E_3	500 - 1500 V
E_4	0.06 E_3
$E_5 = E_7$	0
$E_6 = E_8$	0.04 E_3
E_9	5 - 10 or 120 - 150 V

The anode electrode E_3 controls the emission level; varying the voltages on the downstream focusing electrodes have negligible effect upon the emission current. As the beam enters the Einzel lens it is partially decelerated and forms a virtual image of the source $\sim$2 mm behind the emitter tip. The second Einzel lens focuses the virtual tip image into a $\sim$0.5 mm spot size at the mesh electrode E_9. Further deceleration occurs between electrode E_8 and the mesh E_9. In most cases the mesh was operated between 5 and 10 V relative to the collector thereby providing a nearly field free region between the mesh and the collector at the current threshold. Examination of the spatial characteristics of the beam showed that no significant space charge expansion of the beam occurred down to the cut-off voltage of the mesh. By varying the screen voltage to lower values and measur-

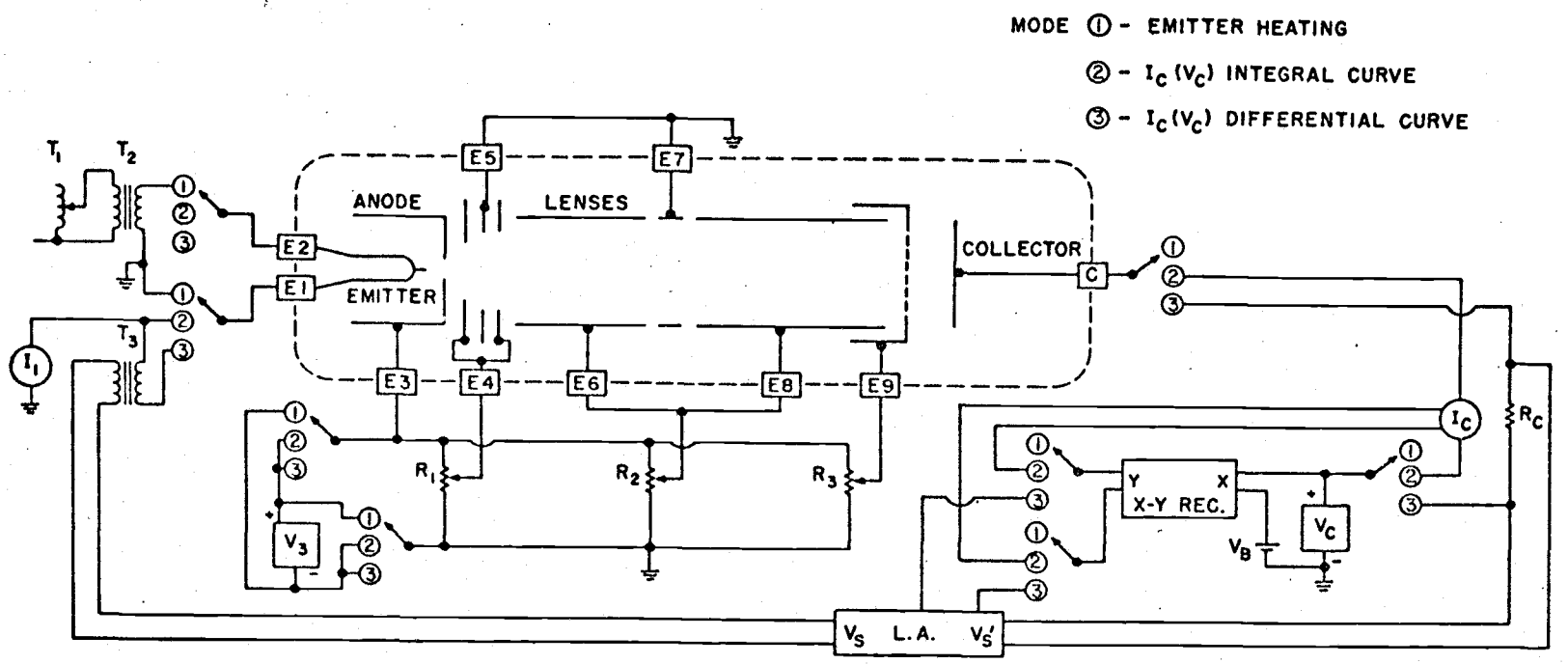

Figure 8. Diagram of the electrical circuitry associated with the FERP tube.

ing the transmitted current in a Faraday cage, the energy distribution curve of the electron beam passing through the mesh was found to be in agreement with the theoretical shape. Also, from the position of the current threshold the mesh work function was found to be approximately 4.6 eV.

The lens system was aligned and mounted securely on four longitudinal glass rods. Both the emitter and anode could be removed as a unit from the tubular anode holder. In this way the emitter, which was held in place by a Corning 1720 glass bead in a molybdenum tube, could be easily replaced and prealigned in the center of the 0.25 mm anode aperture prior to the insertion of the emitter-anode assembly into the anode holder. By positioning the emitter in the plane of the anode aperture, no interception of the primary beam occurred at the anode or subsequent elements of the first lens. Aperturing occurred in the nearly field free region of the second Einzel lens by placing two 1 mm diameter stops in the last lens tube. Thus, electron induced desorbed ions and neutrals from the anode were eliminated, and the high positive saddle at the anode prevented ions generated beyond the first aperture from bombarding the cathode. This design feature greatly improved the current stability without requiring rigorous outgassing of the electrodes. The angular convergence of the beam at the collector was fixed by geometry to be $<1.4^{o}$ for a well focused spot. Hence, negligible loss in resolution resulted from the angular deviation of the beam from perpendicularity at the collector.

The large aperture angle of the analyzer necessarily reduced the resolution of the tube as a retarding energy analyzer. Using the voltage separation between the 10 and 90% points on the leading edge of the energy distribution (Figure 9) as described by Young and Kuyatt (24), the resolution of the gun was determined to vary between 50 and 80 meV, primarily dependent upon anode voltage, emitter orientation

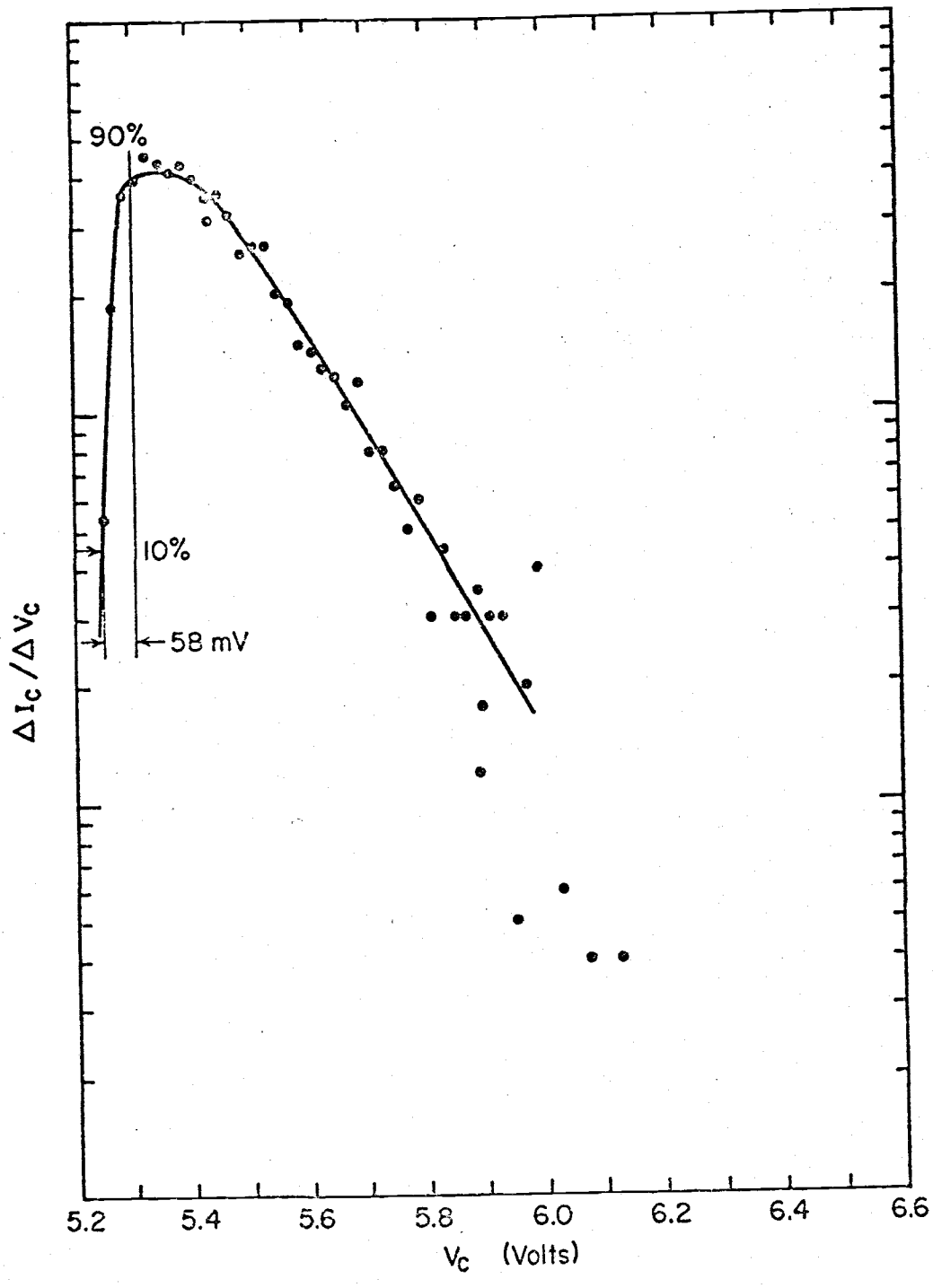

Figure 9. Energy distribution of the collected electrons. The energy difference of 58 meV between 10 and 90% peak height values yields a value of 58 meV for the resolution of the experimental tube.

and position. This resolution was adequate to resolve the leading edge of the energy distribution curve at room temperature.

2. Emitter Fabrication

Two emitters were used for the field electron source in different portions of this study; they were made from <111> and <310> tungsten, both fabricated from zone-oriented wire. Previous studies (7) have shown that electrons field emitted from these orientations exhibit energy distribution curves that agree closely with the Sommerfeld free electron model upon which the theoretical expressions of Chapter II are based. Furthermore, the work functions of the crystal planes intersecting these directions are quite low - 4.3 eV for the (310) plane and 4.4 eV for the (111) plane - thereby providing the highest beam transmission values.

The steps involved in the fabrication of the emitter and its holder are the following:

(1) A 5 mm length (L) emitter blank is cut from a 0.13 mm diameter (D) wire formed by etching in NaOH a 1.25 mm D zone melted tungsten rod of the proper orientation.

(2) The emitter blank is spot welded onto a 0.25 mm D filament etched down to 0.15 mm D in the neighborhood of the emitter blank in order to localize subsequent heating (Figure 10A).

(3) Emitter filament, small pieces of alumina-silicate glass (Corning 1720) and an emitter holder, which is a cylindrical molybdenum tube, are placed in an alignment jig (Figure 10B). The glass is melted in a hydrogen furnace to form a permanent bond between the filament and the emitter holder.

(4) After removing the emitter holder from the alignment jig, the emitter is then placed in 1 N NaOH solution, where it is etched to a sharp point of approximately 1 mm L by applying 10 V DC between the emitter and a nearby electrode (Figure 10C). As the emitter

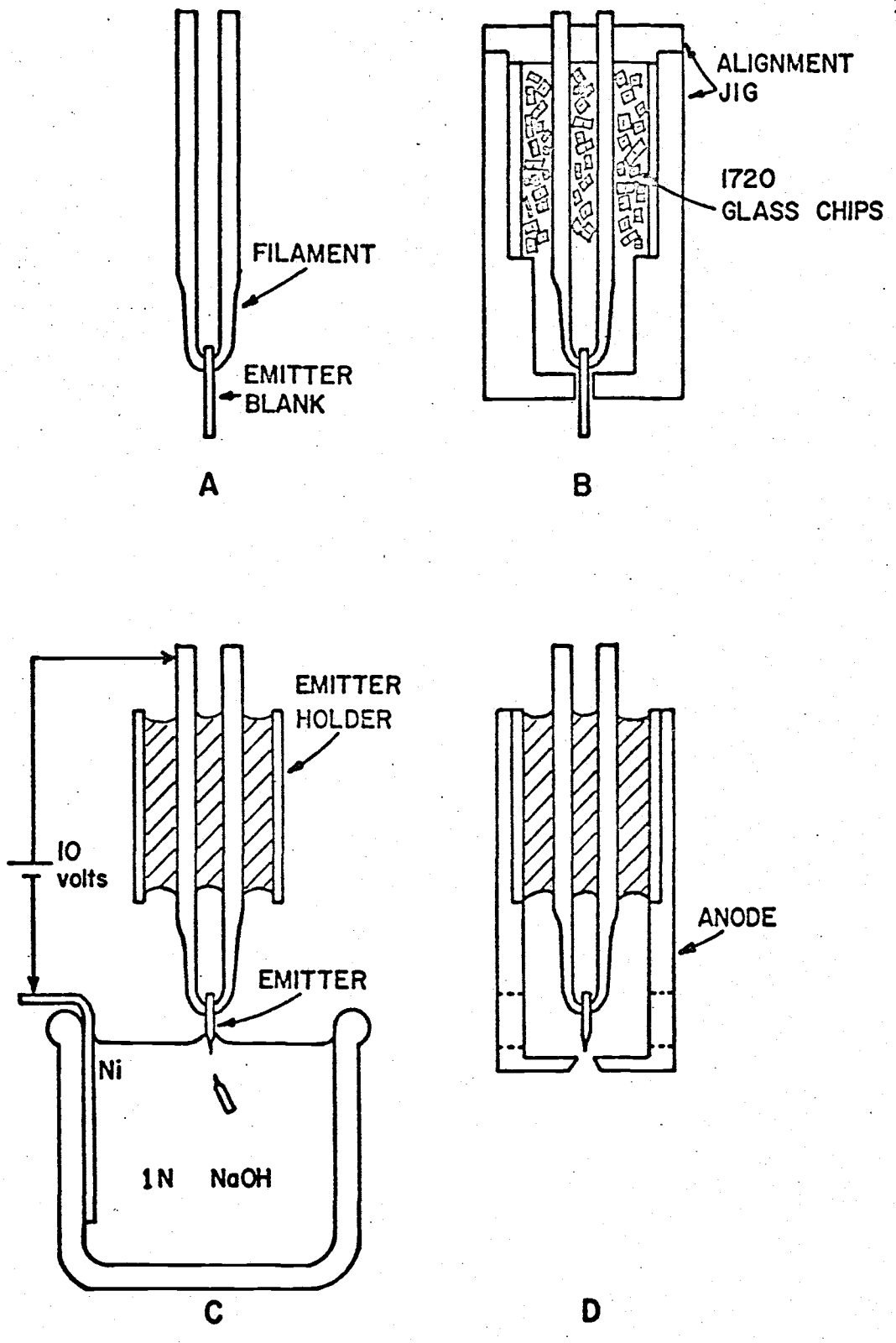

Figure 10. Emitter fabrication: A. Emitter blank spot welded to filament; B. Emitter blank and emitter holder in alignment jig; C. Emitter etching arrangement; D. Emitter-anode assembly.

blank is etched, a point is reached where the emitter blank drops off. At this point the etching is stopped in order to achieve the sharpest possible point. Tip geometry is checked in a 430 power optical microscope.

(5) The emitter holder is then placed in the anode cylinder and alignment of tip and anode aperture is checked by a binocular microscope (Figure 10D).

In this manner the emitter can be placed on the electron optical axis to within $\pm$ 0.001 mm.

3. Collector Fabrication

The collectors were made from single crystal zone refined Marz grade rods obtained from Materials Research Corporation. Typical materials analyses of the rods are given in Table II. The single crystal collector surfaces were fabricated by a high speed grinding wheel and electrochemical machining techniques. Approximately 0.5 mm of the collector surface was removed by electrochemical etching in order to eliminate mechanical defects. The etchant solutions for the nickel, copper, tungsten, niobium and iridium surfaces were concentrated phosphoric acid for both nickel and copper, sodium hydroxide, 25% hydrofluoric, 25% sulfuric acid solution in water, and 5% sodium hypochlorite, respectively. The alignment of the desired crystal directions with respect to target normal was within $\pm$ 1^{o} as shown by Laue X-ray examination. Monocrystallinity of the substrate was carefully checked both before and after measurement by a high powered optical microscope and Laue X-ray examination.

The single crystal collector substrates of this study were shaped and mounted in the holder as shown in Figure 6. The face of the collector crystal was circular with a diameter of 5mm. This was sufficiently large compared to the 0.5 to 1.0 mm beam size to eliminate

TABLE II. COLLECTOR MATERIALS ANALYSES*

Impurity (in ppm)	Collector				
	Cu	Ir	Ni	Nb	W
H	0.016	N.D.**	<1.	<1.0	N.D.
B	N.D.	N.D.	<0.01	0.01	N.D.
C	5.	<3.	17.	35.	<3.
N	<1.	N.D.	<5.	5.0	N.D.
O	2.	<10.	<10.	<10.0	<10.
F	N.D.	<0.3	N.D.	N.D.	N.D.
Na	0.4	N.D.	3.	1.0	<0.5
Mg	<0.4	<4.	0.1	<0.3	0.4
Al	1.	5.	0.2	0.1	<0.5
Si	<2.	3.	<2.	2.0	2.
P	N.D.	<0.2	N.D.	N.D.	N.D.
S	<0.5	<3.	0.5	2.0	0.6
Cl	N.D.	0.4	1.	5.0	0.6
K	0.2	<10.	0.7	0.3	0.2
Ca	0.2	3.	<0.6	0.3	0.3
Sc	N.D.	<0.3	N.D.	N.D.	N.D.
Ti	N.D.	5.	0.04	<2.0	<0.3
V	<0.2	N.D.	N.D.	0.5	<3.
Mn	<0.3	<0.3	<0.1	0.2	0.03
Fe	0.3	15.	15.	2.0	<0.5
Co	<0.3	<3.	<3.	<0.2	N.D.
Ni	<0.4	2.		0.3	0.2
Cu		0.5	5.	7.0	0.1
Zn	N.D.	<0.4	N.D.	N.D.	0.04
Ga	<2.	<0.6	N.D.	N.D.	N.D.
Ge	<1.	<0.6	<4.	<1.0	<0.1
As	<0.3	<1.	0.4	N.D.	N.D.
Se	<2.	N.D.	N.D.	N.D.	<0.1
Br	<2.	N.D.	0.3	N.D.	<0.1
Rb	<0.2	N.D.	N.D.	N.D.	N.D.
Sr	<0.2	<2.	<2.	N.D.	N.D.
Y	<0.4	<2.	<0.3	N.D.	N.D.
Zr	0.4	2.	0.4	0.6	<1.
Nb	N.D.	3.	<0.3		<50.
Mo	<0.2	<5.	N.D.	20.0	5.
Ru	<0.2	100.	N.D.	<0.3	N.D.

TABLE II (CONTINUED)

Impurity	Collector				
	Cu	Ir	Ni	Nb	W
Rh	<0.2	10.	N.D.	<0.3	N.D.
Pd	<0.2	<2.	N.D.	<4.0	N.D.
Ag	<0.4	<3.	N.D.	6.0	N.D.
Cd	<0.3	<6.	<1.	<1.0	N.D.
In	<0.2	<0.6	N.D.	<0.4	<2.
Sn	<0.3	<6.	<6.	<1.0	N.D.
Sb	<0.2	<2.	<6.	<0.3	N.D.
Te	<0.3	<10.	<4.	<1.0	N.D.
I	N.D.	<2.	N.D.	<0.4	N.D.
Cs	N.D.	<0.7	<0.7	N.D.	<2.
Ba	N.D.	N.D.	3.	N.D.	N.D.
Ce	N.D.	N.D.	<0.7	N.D.	N.D.
Nd	N.D.	N.D.	<1.	N.D.	N.D.
Sm	N.D.	N.D.	<1.	N.D.	N.D.
Gd	N.D.	<6.	N.D.	N.D.	N.D.
Yb	N.D.	<10.	N.D.	N.D.	N.D.
Lu	N.D.	<1.	N.D.	N.D.	N.D.
Hf	N.D.	N.D.	<0.3	N.D.	N.D.
Ta	<1.	<10.	<10.	300.0	<3.
W	N.D.	40.	N.D.	25.0	
Re	N.D.	3.	N.D.	N.D.	<2.
Os	N.D.	7.	N.D.	N.D.	N.D.
Pt	N.D.	30.	N.D.	N.D.	<3.
Au	<1.	<1.	<0.7	<6.0	<1.
Hg	N.D.	<1.	N.D.	N.D.	<4.
Tl	N.D.	<10.	N.D.	N.D.	N.D.
Pb	N.D.	1.	N.D.	N.D.	0.4
Th	N.D.	4.	N.D.	N.D.	N.D.

* (28), ** N.D. = Not Detectable. Methods of Analysis: Carbon-conductometric method; gases-vacuum fusion; all others-mass spectograph.

edge effects. Thermal and electron induced desorption cleaning of impurities at the collector crystal were accomplished through electron bombardment. Collector crystals could be easily replaced by removing the glass seal which holds the collector support rod.

B. Instrumentation

1. Circuitry

The circuitry for tube operation is shown in Figure 8. Referring to the diagram, V_c is a Keithley Model 600 A 1000 V, 20 mA digital power supply with an accuracy of $\pm$ 0.05%, $\pm$1 mV, traceable to the National Bureau of Standards. This voltage supply establishes the potential of the collector relative to the emitter and thus determines the accuracy of the work function measurement. The power supply V_3, which determines the anode potential relative to the emitter, is a Fluke Model 410 B 10kV, 10 mA digital power supply with an accuracy of $\pm$ 0.25% $\pm$ 250 mV. Since this supply is not in the emitter-collector circuit, its accuracy is not critical, but its stability ($\pm$ 0.05% $\pm$ 50 mV) is important for constant electron emission. The resistors R_1, R_2 and R_3, which provide the potential on the lens elements of the tube are each Kelvin-Varley resistance divider networks (see Figure 11). These resistor networks allow the potentials on the lens elements to be set to 1 part in 10^4 of the anode potential. Since one side of the resistor networks is connected to E_3, the anode potential, the potentials on the lens elements vary in direct proportion to the potential of the anode; thus the electron paths through the focusing elements remain independent of any change in the current-voltage characteristics of the emitter.

The meter I_c is a Keithley Model 600 A battery-operated electrometer; I_1 is a Keithley Model 610 B line-operated electrometer. Both meters have an accuracy of $\pm$ 3%. The important feature of

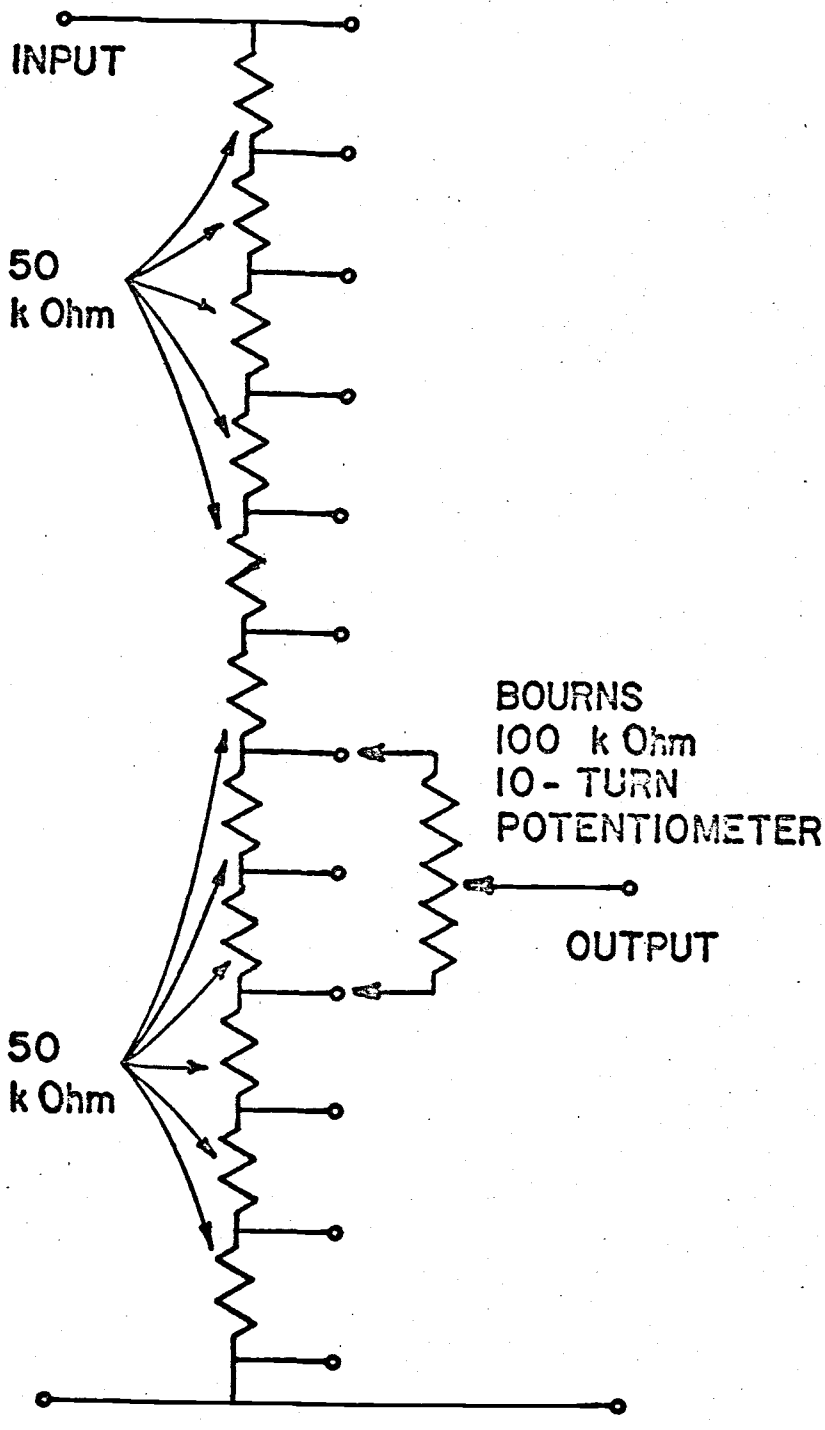

Figure 11. Kelvin-Varley divider network for resistances R_1, R_2 and R_3.

these meters is that they have a "FAST" or feedback mode of operation for which the potential difference across the meter leads is 1 mV or less; since they are both in the emitter-collector circuit, it is important that this potential difference be minimized. It is essential that meter I_C be battery operated because it is operated at the collector potential.

A Princeton Applied Research Model HR-8 Lock-In-Amplifier (LA in Figure 8) is used to provide a differential of the collector current-voltage curve. It provides a 10 mV, 1000 Hz signal, V_S, to the emitter through transformer T_3 and detects the same frequency signal, V'_S, by measuring the collector current through R_C. The magnitude of V_S is proportional to the slope of the $I_C(V_C)$ curve as a function of collector voltage.

By proper connections (see Figure 8) either the collector current or its differential could be recorded as a function of collector potential on an Electronics Associates, Incorporated, Model 1120 10 in by 15 in X-Y recorder. The accuracy on each scale is 0.25%.

In order to clean the emitter surface the emitter is heated by passing AC current through the supporting filament. The current is provided by a variable transformer T_1 and a 6.3 V AC filament transformer T_2.

2. Evacuation Systems

The experimental tube was evacuated on a liquid nitrogen trapped mercury diffusion evacuation system that was bakable to 400°C. After outgassing the collector and nearby elements by electron bombardment, vacuum in the 10^{-10} torr range was routinely obtained. The experimental tube was surrounded by a magnetic shield to reduce the effect of stray magnetic fields.

IV. EXPERIMENTAL PROCEDURE

Each collector target was fabricated and, in its turn, mounted in the experimental tube, as described previously. After mounting the collector substrate, the tube was evacuated to $\sim 10^{-10}$ torr pressure range. The arrangement allowed for the option of immersing the tube partially or completely in liquid nitrogen in order to enhance the vacuum stability and to extend the temperature range of the work function measurements.

Cleaning of the crystal surface was accomplished by electron bombardment heating to 2100°K for niobium and tungsten, 1700°K in the case of iridium, 1400°K for nickel and 1100°K for copper. The copper crystal was exposed to 10^{-6} torr of hydrogen and heated to 1250°K. In order to remove potential carbon contamination the nickel crystal was first heated in 10^{-5} torr of oxygen followed by heating in 10^{-6} torr of hydrogen and then heated to ~ 1400°K in high vacuum. Thermal heating was continued until the field electron emitter, which was also cleaned thermally (mode 1 in Figure 8) and therefore very sensitive to gas release from the collector, showed no change in current after flashing the collector substrate to its cleaning temperature. As a corollary check, the absence of further change in the collector work function on heating was used as an indication of a clean surface.

The emitter-to-collector current-voltage characteristics were taken several times for each collector crystal and plotted on an X-Y recorder (mode 2 in Figure 8). A computer program (Appendix II) was formulated to plot the data according to Equation (9) so that a value of ϕ_c and d could be obtained. As will be noted later this method of determining ϕ_c and d was not always applicable due to reflection. Therefore, the differential curve was also taken by utilizing the mode 3 circuitry in Figure 8, which involves the well known electronic differentiation method utilizing the lock-in-amplifier described pre-

viously. The resulting plot of dI_c/dV as a function of V_c is the total electron energy distribution as measured at the collector. From the position of the TED peak and Equation (11), a value of ϕ_c was obtained; this result could be obtained with an experimental accuracy of ± 20 meV. The I-V and TED data were usually taken at emitter temperatures of 77°K and 300°K.

V. EXPERIMENTAL RESULTS

The values of ϕ_c obtained by the FERP method are reported in Table III along with a comparison with other methods and with values calculated from a semi-empirical method developed by Steiner and Gyftopoulos (29). The FERP values were obtained via Equation (11) from the TED curves shown in Figures 12 - 14. An interesting feature of these results is the additional structure in the TED for Cu(100), Nb(100) and to a lesser degree for Ir(111). This anomalous structure near the threshold of the TED curve was not as apparent in the other results and was determined to be due to unusual electron reflection. The integral current-voltage characteristics shown in Figures 15 - 22 on a compressed voltage scale clearly show that the origin of the TED structure in Cu(100) and Ir(111) is due to electron reflection which varies rapidly at the threshold voltage. Although the integral curve for Nb(100) was not obtained due to inadvertent melting of the crystal, the structure in the TED curve suggests a reflection coefficient which also varies rapidly near threshold. All other substrates show reflection at threshold, but to a lesser degree.

If it is assumed that all the reflected electrons are collected at the mesh, the sum of the collector current I_c and mesh current I_s is given by

$$I'_p = I_c + I_s, \tag{13}$$

where I'_p is the emitter current arriving at the mesh. Noting that the mesh transmission is given by $I_p/I'_p = T$, where I_p is the current impinging on the collector, and that $(1 - R) = I_c/I_p$, one obtains

$$(1 - R) = I_c/T\,(I_c + I_s). \tag{14}$$

TABLE III. COMPARISON OF VALUES OF ϕ_c OBTAINED BY FERP METHOD AND BY OTHER METHODS

Material	Atom Density (atoms/cm^2)	Work Function (eV)				
		This Work	Thermionic	Photoelectric	Field Emission	Calculated
W(110)	14.1	5.25 ± 0.02	5.35 ± 0.05[30]		5.9 ± 0.1[7]	5.50
W(100)	10.0	4.63 ± 0.02	4.60 ± 0.05[30]		4.70 ± 0.05[7]	4.66
W(111)	5.77	4.47 ± 0.02	4.40 ± 0.02[30]		4.45 ± 0.03[7]	4.47
Ir(111)	15.8	5.76 ± 0.04	5.79 ± 0.03[31]			5.56
Ir(110)	9.7	5.42 ± 0.02				4.84
Nb(100)	10.9	4.18 ± 0.02	3.95 ± 0.03[32]		3.87 ± 0.01[33]	4.08
Ni(100)	16.15	5.53 ± 0.05		5.22 ± 0.04[34]		5.56
Cu(100)	15.4	5.10 ± 0.05	4.9[35]			4.99

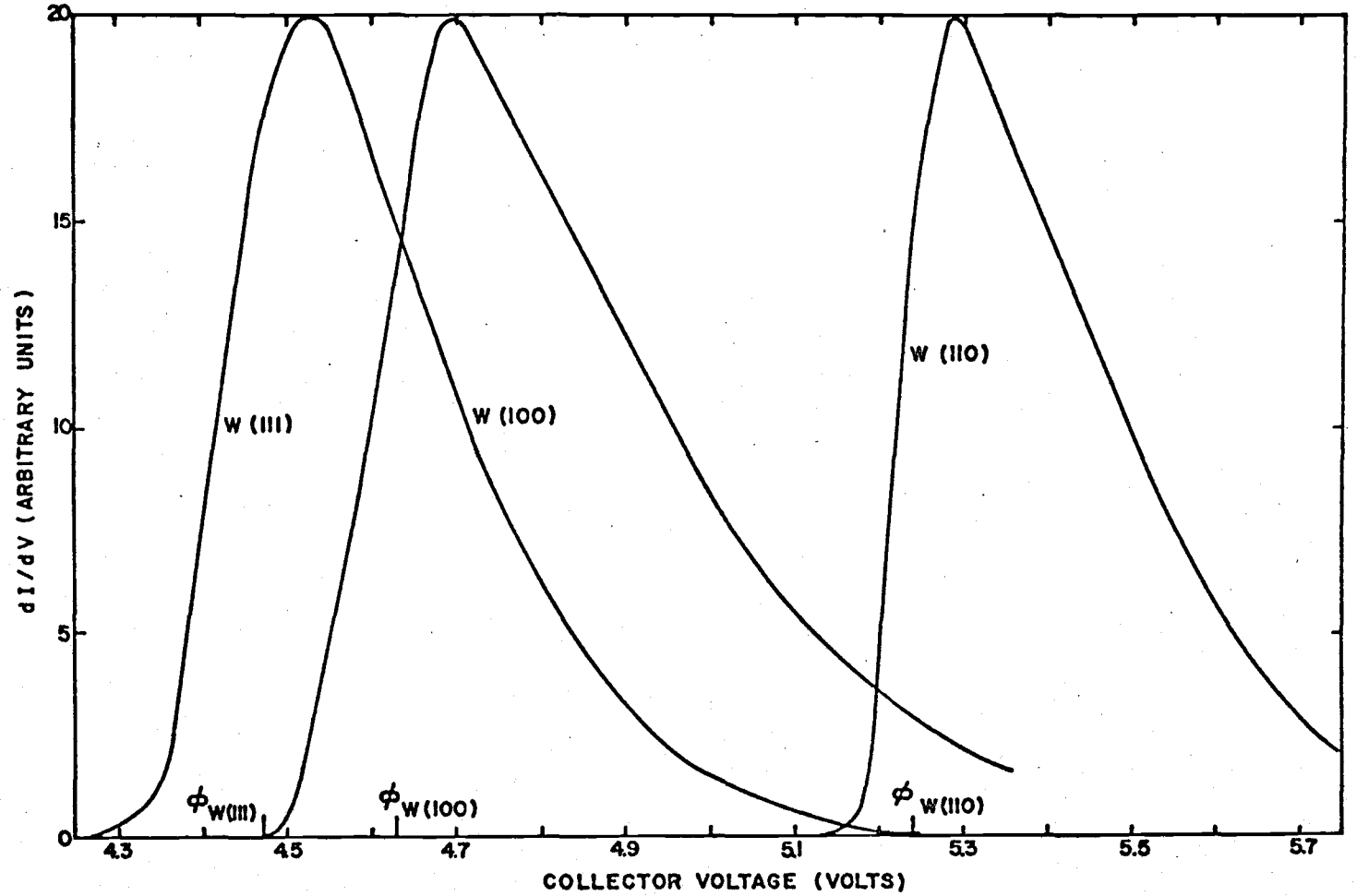

Figure 12. TED curves for W(111), W(100) and W(110).

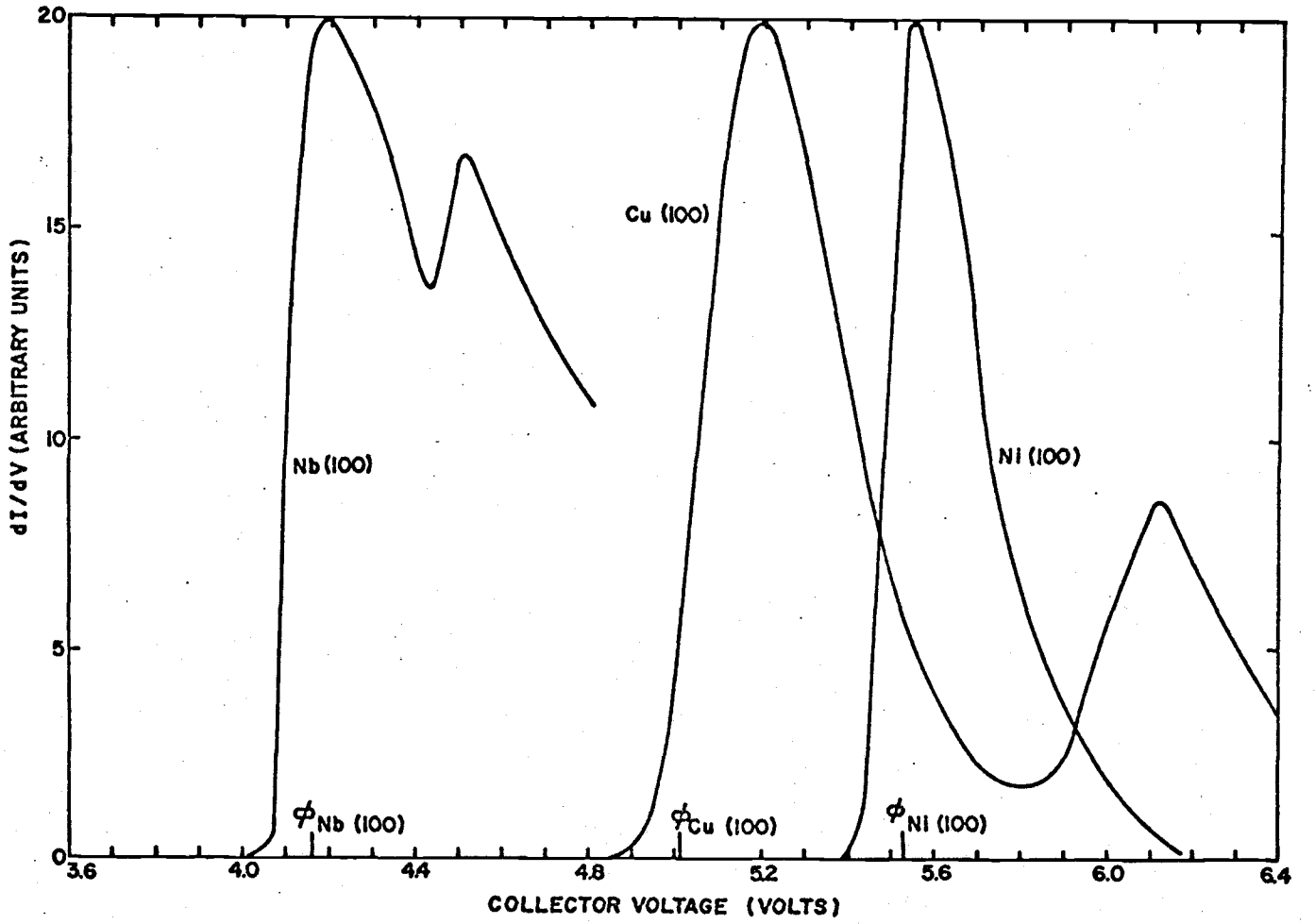

Figure 13. TED curves for Cu(100), Ni(100) and Nb(100).

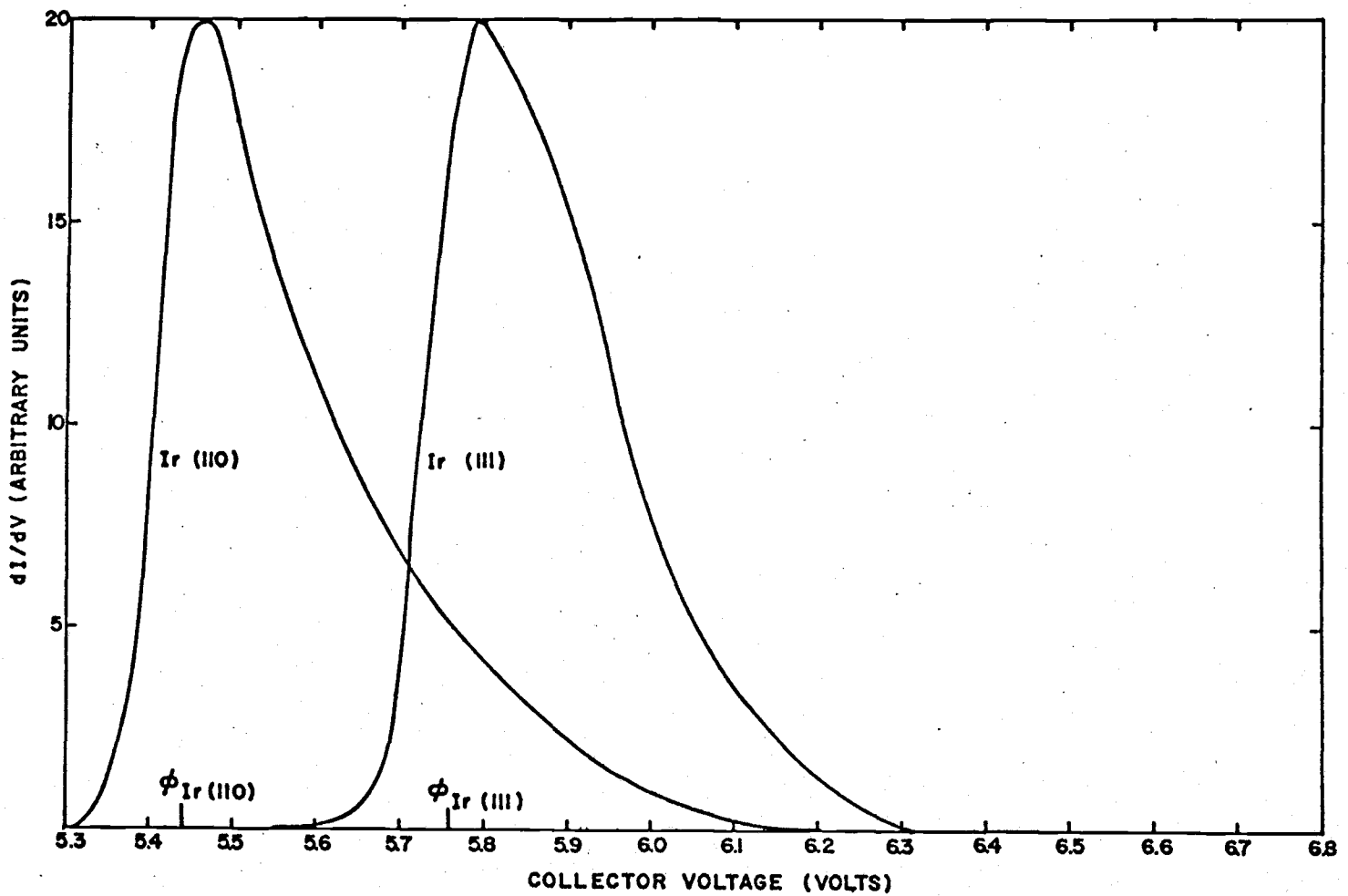

Figure 14. TED curves for Ir(111) and Ir(110).

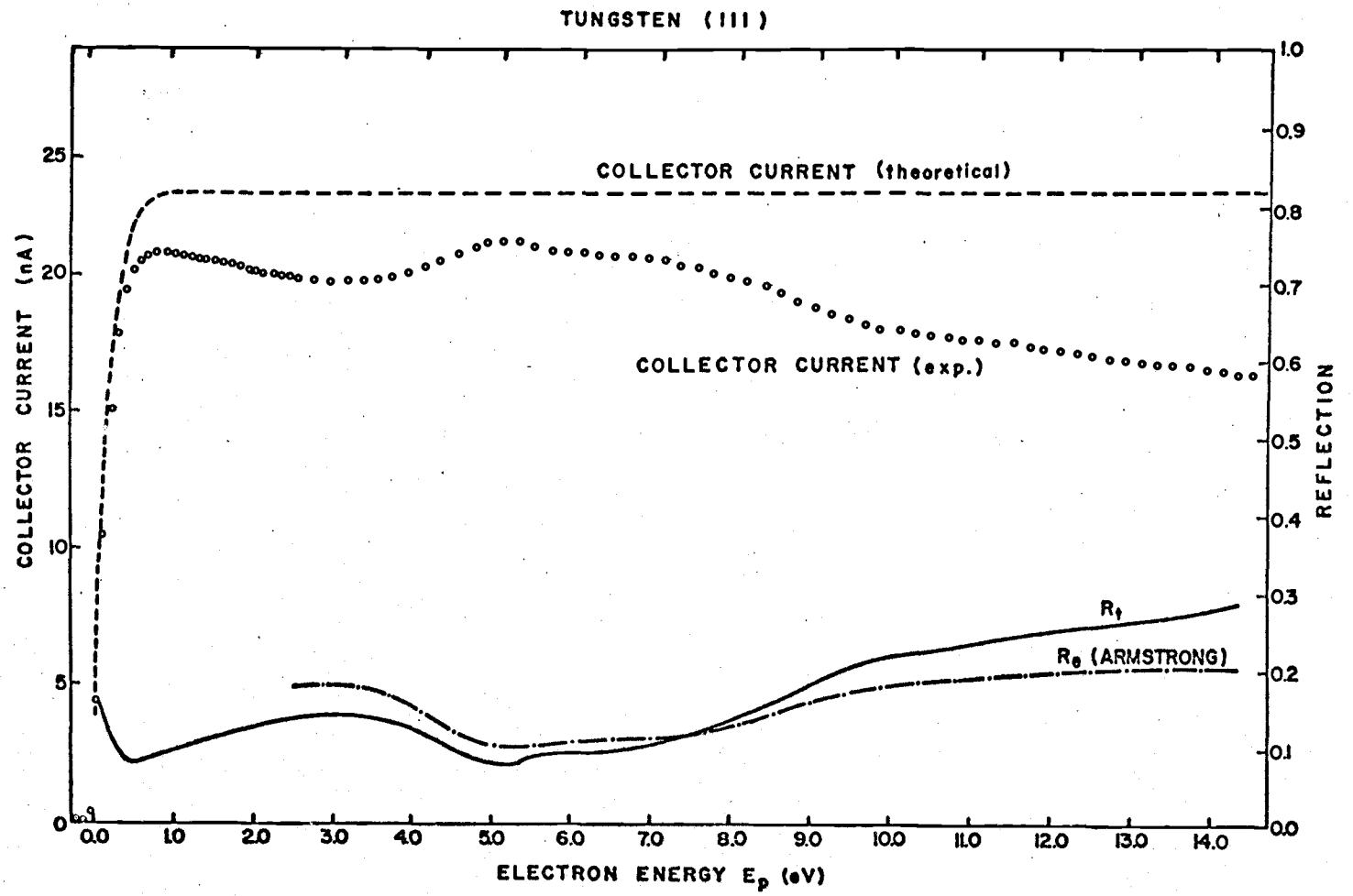

Figure 15. Experimental and theoretical integral $I(V_c)$ curves obtained from W(111). Solid lines shows the total reflection curve R_t. Dashed curve gives the experimental elastic reflection curve R_e obtained by Armstrong (46).

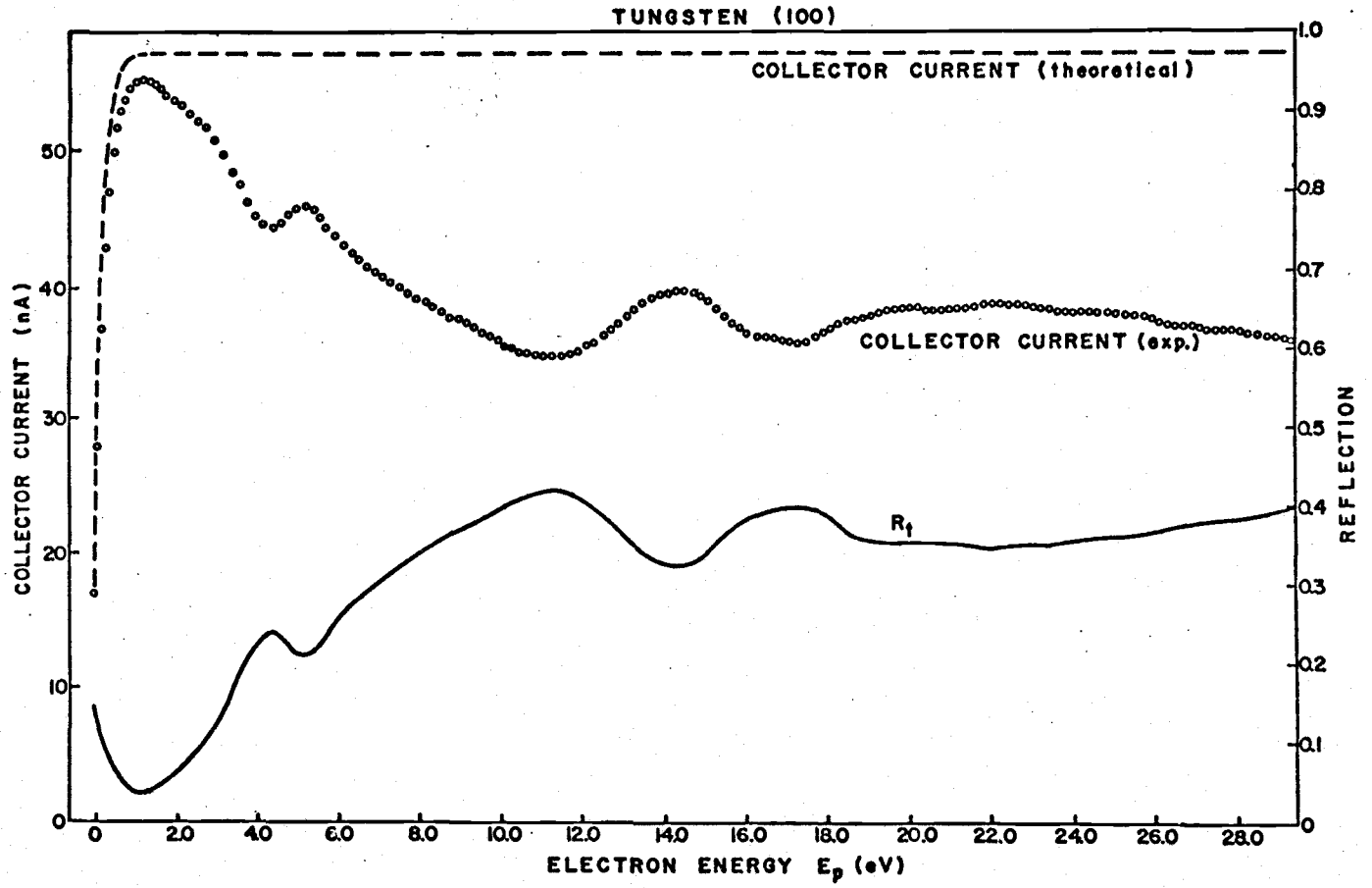

Figure 16. Experimental and theoretical $I(V_c)$ curves obtained for W(100). Solid line shows the total reflection R_t curve. The mesh voltage V_s = 100 V.

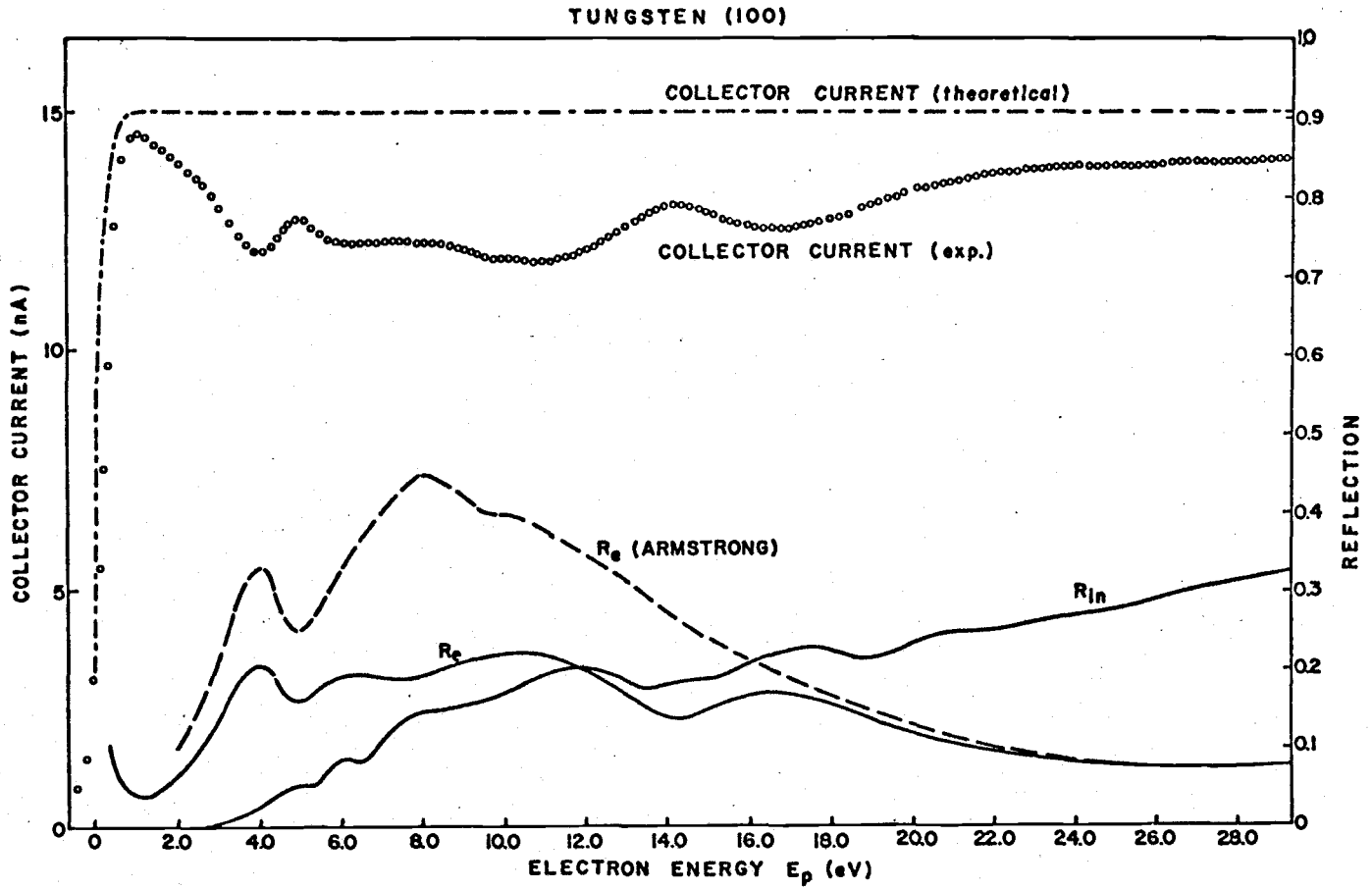

Figure 17. Experimental and theoretical $I(V_c)$ curves obtained from W(100). Solid line curves show inelastic R_{in} and elastic R_e reflection coefficients. The mesh voltage V_g = 5.25 V.

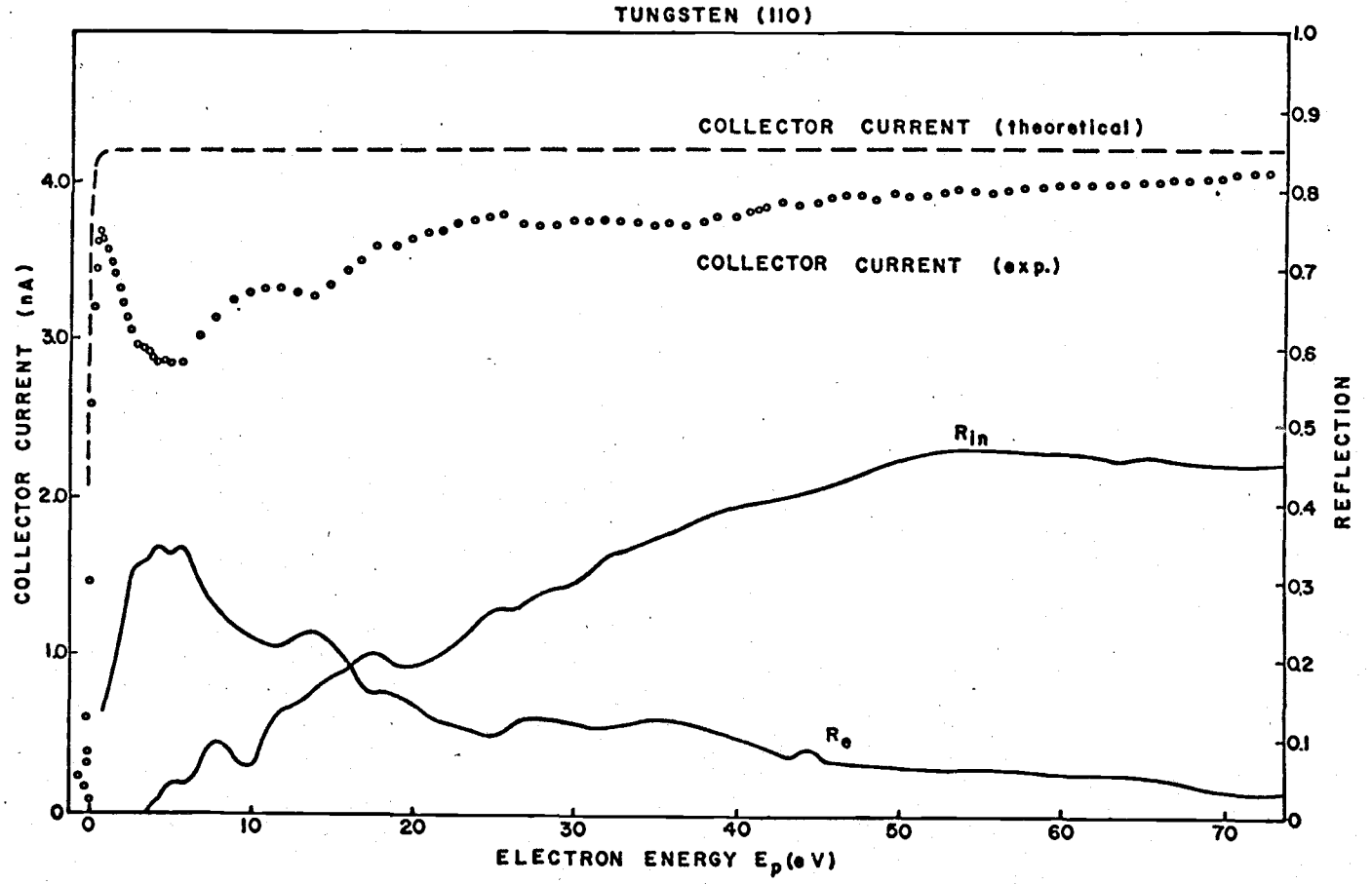

Figure 18. Experimental and theoretical $I(V_c)$ curves obtained from W(110). Solid line curves show inelastic R_{in} and elastic R_e reflection coefficients.

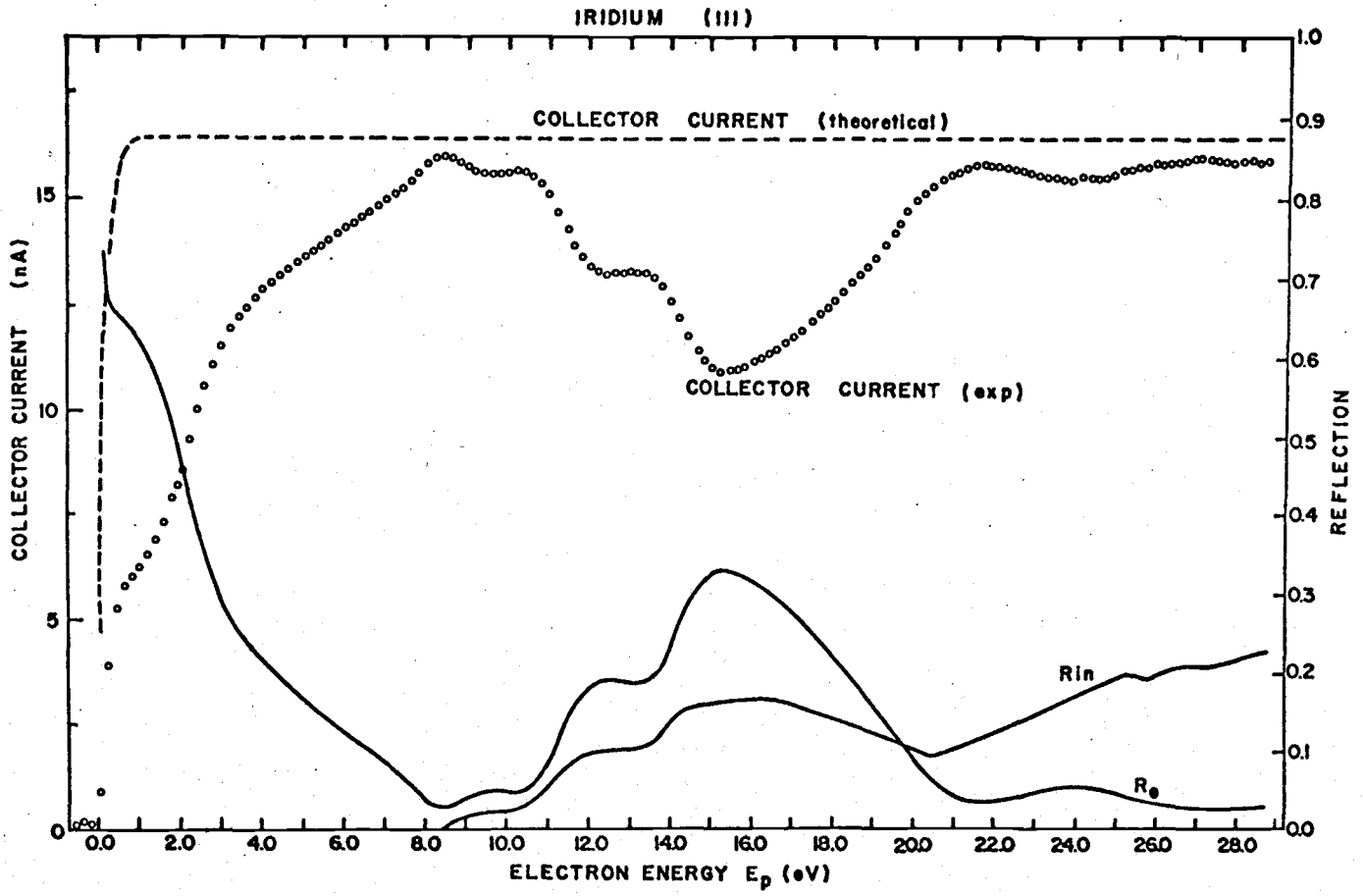

Figure 19. Experimental and theoretical $I(V_c)$ curves obtained from Ir(111). Solid line curves show inelastic R_{in} and elastic R_e reflection coefficient curves.

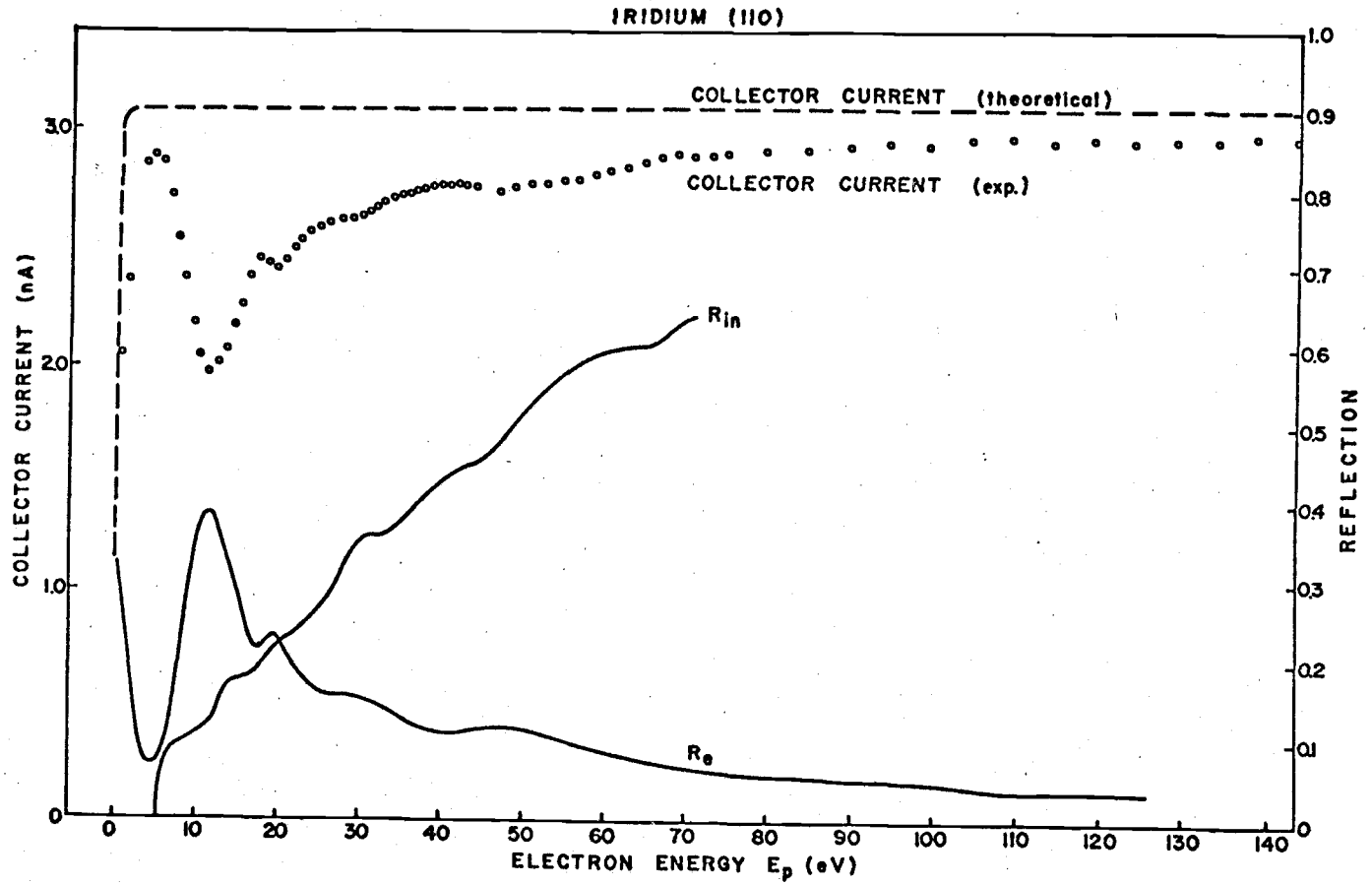

Figure 20. Experimental and theoretical $I(V_c)$ curves obtained from Ir(110). Solid line curves show inelastic R_{in} and elastic R_e reflection coefficients.

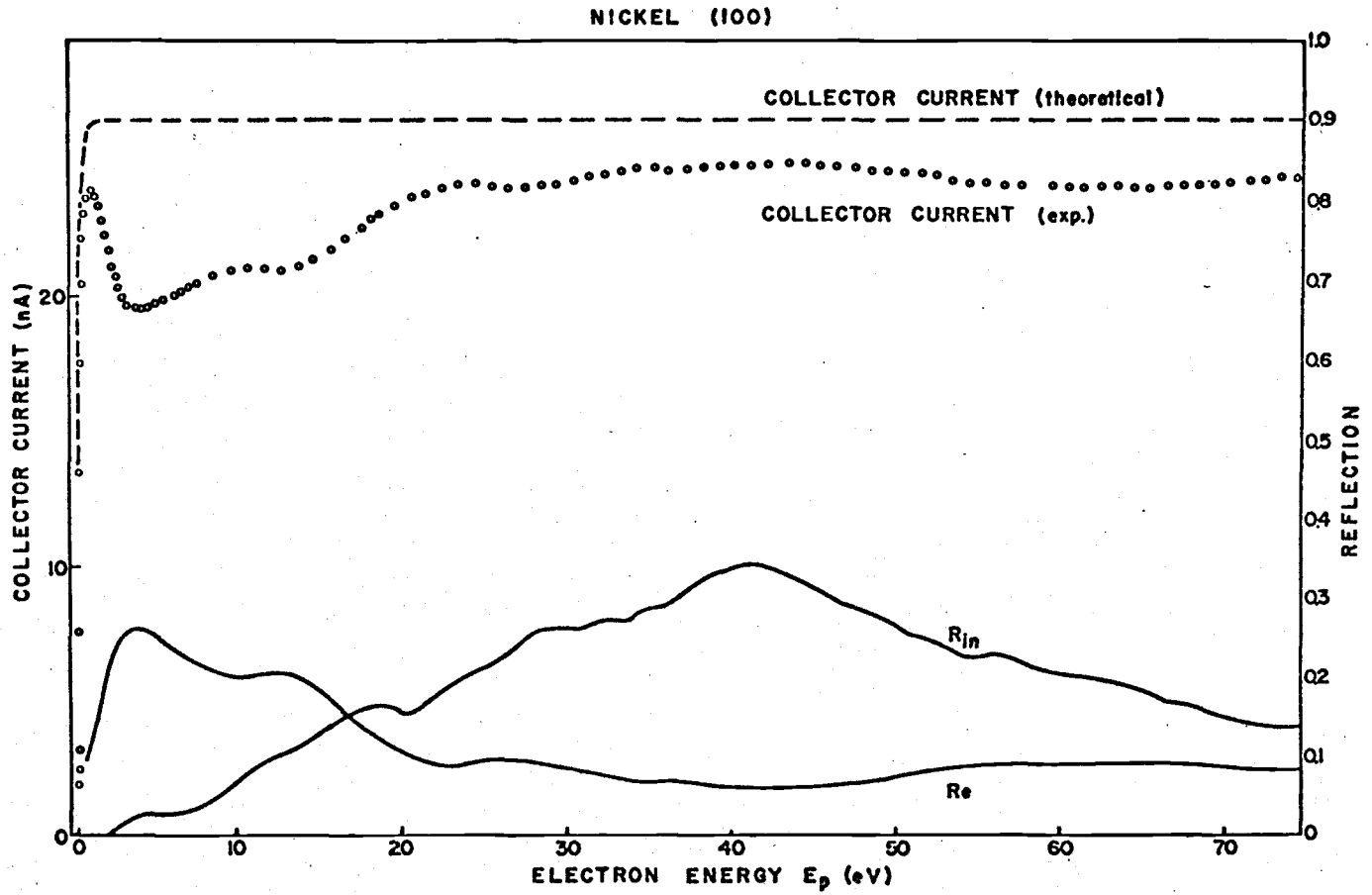

Figure 21. Experimental and theoretical $I(V_c)$ curves obtained from Ni(100). Solid line curves show inelastic R_{in} and elastic R_e reflection coefficients.

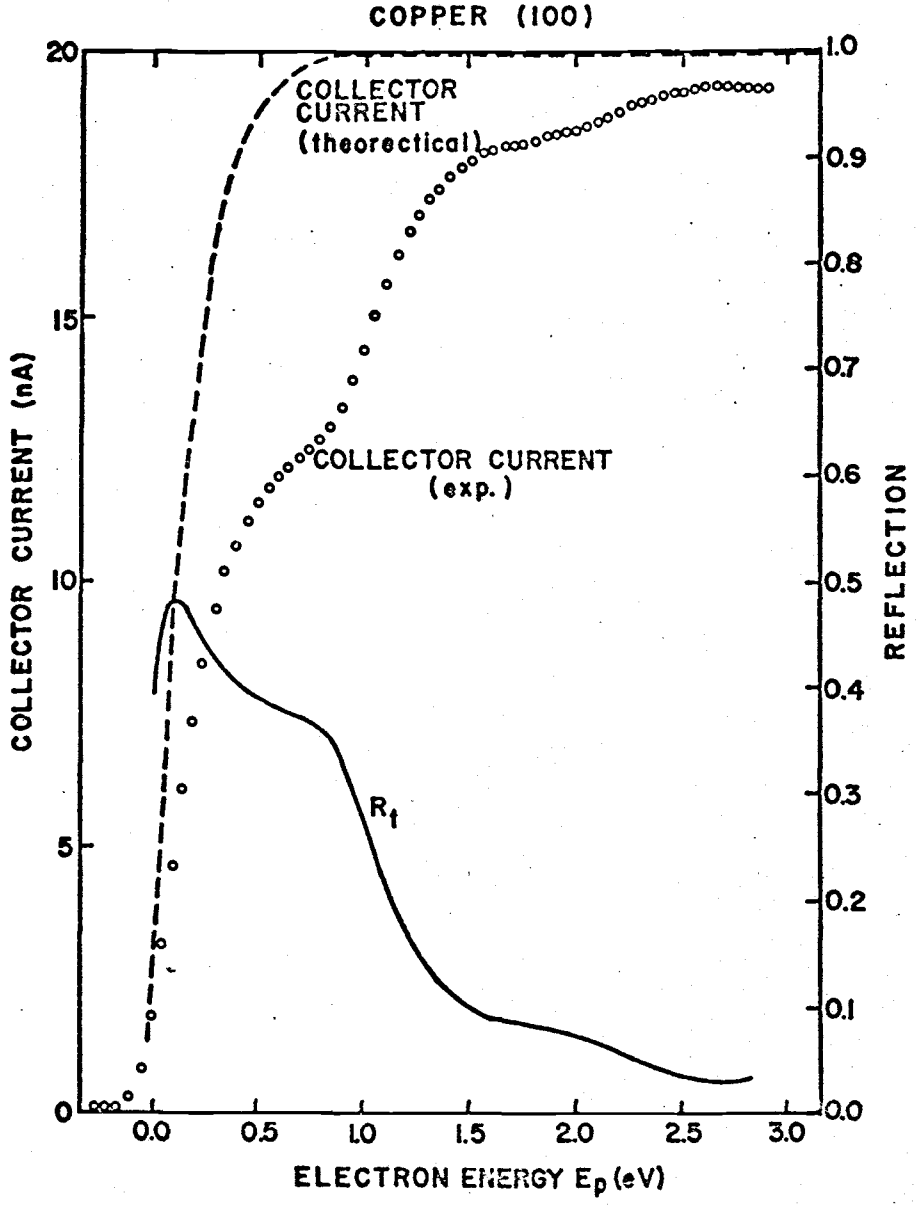

Figure 22. Experimental and theoretical $I(V_c)$ curves obtained from Cu(100). Solid line curve shows the total R_t reflection coefficient.

Since T, I_c and I_s are measurable quantities R may be determined as a function of V_c as shown in Figures 15 - 22 for each of the substrates. It is important to point out that Equation (14) is valid when I_p is at its saturated value. Since we do not wish to count electrons reflected by the retarding field, it is necessary to use the theoretical variation of I_p with V_c to calculate R in the retarding range. As a self consistent check on the electron current accounting we can also measure I'_p in the deep retarding range preceding the threshold where $I'_p = I_s$; this value of I'_p generally agreed with that calculated from Equation (13) at saturation. The theoretical dependence of the current I_p on V_c is also plotted in Figures 15 - 22 with appropriate normalization factors applied. Clearly the values of R for both Ir(111) and Cu(100) are unusually high and rapidly changing near threshold. It must be remembered that the energy spread of the primary beam at half height is ~ 0.2 eV so that structure in R less than 0.2 eV width may be detected but not accurately reproduced with respect to shape. However, with these definitions in mind, one may confidently measure R down to zero primary beam energy. It should be pointed out that in order to obtain the value of the primary beam energy ϕ_c must be subtracted from the abscissa of each of the I-V curves. The latter correction has been made in Figures 15 - 22.

In the experimental setup when $V_c - \phi_c > V_s - \phi_s$ (s refers to the screen-mesh electrode) those reflected electrons which lose energy through inelastic processes will not be collected at the mesh but instead will be returned to the collector. Thus, by fixing $V_s = 5.8$ V, only specularly reflected elastically scattered electrons will escape from the collector crystal. The elastically reflected electron coefficient R_e has been measured for several substrates as given in Figures 16 - 21. By setting $V_s \simeq 130$ V all reflected electrons in the energy range investigated return to the mesh and total

reflection R_t curves are obtained (see Figure 15). Hence, it is possible by this technique to measure the inelastically reflected electron coefficient R_{in} by noting that $R_{in} = R_t - R_e$. In Figures 16 - 21 values of R_{in} are given for several of the crystal faces. For the crystal faces Cu(100) and W(111) only R_t values were obtained. Difficulty with leakage current to the mesh electrode caused some minor uncertainty regarding the absolute values of R for Ir(110), W(110) and Cu(100).

VI. DISCUSSION

A. Work Function

1. Comparison with Other Measurements

As shown in Figure 12 and Table III the work function values of 4.47, 4.63 and 5.25 eV obtained for the (111), (100) and (110) planes of tungsten are in close agreement with values reported by other methods, particularly thermionic and field emission methods. Since the electron reflection coefficient is low (less than 15%) near the threshold for the tungsten results, the values of ϕ_c obtained from Equation (9) compare within experimental error with the values computed from the TED curves via Equation (11) (see Figure 3 for a typical result utilizing Equation (9)). This merely provides the expected self consistent check on the experimental method when R is small or a slowly varying function of energy near threshold.

Notable is the well known discrepancy between ϕ(110) obtained on macroscopic crystals and microscopic crystals employed in field emission (i.e., by use of the Fowler-Nordheim (FN) equation) techniques. This discrepancy is believed to be due to large geometric facets which occur on W(110) planes of a field emitter and which can alter the FN results in the observed fashion. Tungsten work function values exhibit the usual increase with surface atom density in accordance with the semiquantitative theoretical expectations of Smoluchowski (36).

The Ir(111) plane, possessing one of the highest atom densities, yields the expected high work function value $\phi = 5.76$ eV as shown in Figure 14. A similar high value of ϕ for Ir(111), in remarkable agreement with the value obtained here, has been reported by Zandberg and Tontegods (31) who observe this to be the highest work function reported for a macroscopic single crystal metal surface. The

agreement is surprising in view of the initial polycrystalline nature of Zandberg and Tontegode's iridium crystal. The results of this work indicate that this crystal face is relatively stable with respect to thermal induced recrystallization and faceting effects such as observed on the high work function Re(0001) face (37).

The Ir(110) work function is somewhat lower than Ir(111) as expected on the basis of the lower atom density. Considering that the (110) face of Ir is the third most densely packed plane, the relatively large value $\phi = 5.42$ eV is indicative of the generally high work function of all crystal faces of iridium.

The value of $\phi = 4.18$ eV for the (100) face of niobium, which has a body centered crystal structure, shown in Figure 12 agrees closely with thermionic and FN values reported by others (32,33). (See Table III). The work function values for W(100) and Mo(100) obtained by a variety of methods indicate best values of 4.65 and 4.40 eV respectively (33). Both W(100) and Mo(100) possess identical atom densities $\sigma = 10.9 \times 10^{14}$ atoms/cm^2. Since molybdenum and niobium are neighboring elements in the periodical table one might expect geometric factors to dominate thereby causing a larger ϕ for niobium. This is obviously not the case. These results underscore the role of electronic factors in the variation of work function with crystal face and material.

Few reliable values of work function for the (100) face of nickel and copper are reported in the literature - obviously, due to the surface cleaning difficulties. The results of this work, shown in Figure 13 and Table III are in rough agreement with photoelectric (34) and thermionic (35) values reported for Ni(100) and Cu(100), respectively. Using careful cleaning procedures and a gold reference electrode, Delchar (38) reports a work function value of 5.16 eV for Cu(100) in excellent agreement with this work. Delchar points out that any

possible error in the work function value for the reference electrode would likely be in such a direction as to raise the Cu(100) value.

The value of Ni(100) work function in this experiment is 0.30 eV larger than any other reliable measurements. Most previous measurements on crystals of questionable surface purity converge on a value of 4.9 eV. Clearly, a combination of the FERP method with Auger analysis would be extremely helpful in answering the question fo surface cleanliness.

2. Comparison with Work Function Calculations

During the past few years, there have appeared a number of papers concerned with calculation of the work function. These may be divided into (1) efforts aimed at the formulation of a first principles description of the work function (3,39-41) and (2) empirical correlations relating the work function to other metallic properties (29,42,43).

The first principles approaches start with the "jellium" or free-electron model, with refinements, and are useful for calculations of work functions for the alkalis and other simple metals. However, their predictions for the work functions of noble and transition metals show large discrepancies with experiment, due to the neglect of structural and electronic factors. For example, it is interesting to note that the elements copper and molybdenum are each adjacent to nickel and niobium respectively in the periodic table. In each case the change in the free atom electronic structure between adjacent elements involves the filling of the inner d orbitals. In the case of fcc metals nickel and copper the work function of the (100) crystal face decreases with atomic number Z, whereas with the bcc metals niobium and molybdenum the work function of the (100) face increases with Z. At the same time each of these pairs of metals exhibits a

slight increase in their respective lattice constants with Z. The value of the (100) work function for the body centered crystal metal tungsten is larger than the molybdenum value by ~ 0.25 eV even though both metals posses nearly identical lattice constants and differ in electronic structure by the filling of inner 5p and 4f orbitals. Clearly, a predictive theory of metallic work function must include complex structural and electronic factors.

In contrast, a recent semi-empirical formulation by Steiner and Gyftopoulos (29) makes use of the concept of electronegativity to derive an equation by which quantitative values of $\emptyset$ may be calculated with a minimum of assumptions. In this work, $\emptyset$ is defined in terms of the amount of work required to remove an electron from a valence orbital of a surface without altering the energy state of the atoms. This reduces the problem of calculating the work function to that of computing the energy per valence electron in a surface atom. By equating $\emptyset$ with the neutral orbital electronegativity, the following expression for $\emptyset$ is derived (29):

$$\emptyset = 0.98 \frac{v_s + 1}{r_m} + 1.57 \quad \text{(eV)} \tag{15}$$

where v_s is the number of bonding electrons per surface atom, and r_m, the effective size of these atoms in angstroms, is assumed to be equal to the atomic radius (44).

In order to use Equation (15) for calculating $\emptyset$, Steiner and Gyftopoulos derive the surface valence v_s in terms of the metallic valence v_m and the fractional bond numbers of atoms in the bulk. A brief outline of the method is presented in the following paragraphs.

The number of bonding electrons per atom in the bulk of a metal is defined as the metallic valence v_m. The average number of bonding electrons shared by two interacting atoms separated by a distance R is 2n, where n is the fractional bond number (45). Ac-

cording to Pauling (46), the fractional bond numbers n_a and n_b associated with the interatomic separations R_a and R_b is given by:

$$R_b - R_a = 0.26 \ln (n_a/n_b). \tag{16}$$

For bcc and hcp crystal structure, fractional bond numbers between atoms further distant than next nearest neighbors are negligible. For fcc fractional bond numbers between atoms further distant than nearest neighbors are negligible. The metallic valence and fractional bond numbers for the various crystal structures are given by:

$$\begin{aligned} v_m &= 8n_a + 6n_b && \text{for bcc} \\ v_m &= 6n_a + 6n_b && \text{for hcp} \\ v_m &= 12n_a && \text{for fcc} \end{aligned} \tag{17}$$

where n_a and n_b are the fractional bond numbers for nearest and next nearest neighbors, respectively. Tabulated values of metallic valence and interatomic distances can be used in Equations (16) and (17) to compute the fractional bond numbers n_a and n_b. If it is assumed that the fractional bond numbers of atoms on the surface are identical to those of atoms in the bulk, then the surface valence is given by:

$$\begin{aligned} v_s &= N_a n_a + N_b n_b && \text{for bcc and hcp} \\ v_s &= N_a n_a && \text{for fcc} \end{aligned} \tag{18}$$

where N_a and N_b are the number of nearest and next nearest neighbors of surface atoms respectively. The numbers N_a and N_b are fixed by the crystallographic orientation of the surface.

The semi-empirical approach outlined above allows for computations of ϕ to be made based on known properties of metals. Following this procedure work function values for the metals and orientations of this work were computed and are listed in Table III. The calculated values agree with experiment to within 5%. This remarka-

bly good agreement reemphasizes the observation that the electronic structure of the surface is significant in predicting the clean work function of the surface. The most significant factors in determining the work function of a metal surface according to this theory are the number of ligands possessed by an atom on the surface, the interatomic distances between that atom and its ligands, and the metallic valence. The high work function planes are those for which the number of ligands and the metallic valence are large, and the interatomic distances are small.

B. Electron Reflection

The simultaneous measurement of work function and electron reflection was undertaken here primarily as a further index of surface cleanliness. The ease of separating the elastic R_e and inelastic R_{in} reflection coefficients by this method motivated a more detailed study of these coefficients as a function of the primary electron energy E_p. Several interesting and surprising features have been observed in the variation of R with E_p in the low energy range.

Figure 15 shows that the variation of R_t with E_p for W(111) is in good agreement with careful measurements of R_e by Armstrong (47). Because of the ability of the FERP method to accurately measure R to within a few tenths eV of threshold, these results show a definite peak at 3 eV heretofore unobserved. A small peak observed at 6 eV is in agreement with Armstrong's results. Disagreement in absolute scale at larger values of E_p can be ascribed to the difference between Armstrong's measurement of R_e and, in this work, the measurement of R_t for this crystal face. As also shown in Armstrong's results surface contamination markedly alters R_e; thus the close agreement between the two results mutually supports the claim of an atomically clean surface.

The W(100) results in Figures 16 and 17 show the experimental variation of I_c with E_p for $V_s = 100$ and 5.25 V respectively, thereby illustrating the difference between the total and elastic reflection modes. In Figure 17 the value of the experimental reflection coefficients R_{in} and R_e are given along with Armstrong's results for R_e. Both results agree that a sharp peak R_e occurs between 3.5 and 4.0 eV as observed similarly in the W(111) results. In disagreement with Armstrong's results, the large peak in R_e at 8.0 eV is missing and instead a smaller peak at 6.5 eV appears. In addition, a major peak observed in these results, but absent in Armstrong's, occurs at 16.5 eV. (Earlier results by Kahn, Hobson and Armstrong (48) show a definite peak in this energy range.) Both investigations agree on a broad peak in R_e at 10.5 eV. Differences in the R_e versus E_p curves obtained in the two investigations must be ascribed to either a small degree of surface contamination, crystal inhomogenity or experimental artifact.

The variation of R_e with E_p for W(110) shown in Figure 18 over a wider E_p range exhibits a large peak modulated with fine structure in the 4 - 6 eV range. Lesser peaks occur at 14 and 27 eV as R_e decreases from a peak value of 0.34 at 5 eV to less than 0.03 at 75 eV. The W(110) R_e curve agrees closely with an earlier result by Kahn, Hobson and Armstrong (48).

The inelastic reflection coefficients R_{in} given in Figures 17 and 18 for W(100) and W(110) exhibit very similar structure for both crystal faces. That is, each exhibits an onset threshold at 3 eV, fine structure in the 3 to 10 eV range, and additional peaks at 12 and 17 eV. The larger range of E_p for W(110) indicates an increase in R_{in} to a value of 0.47 at 52 eV where it then begins a slight drop. The R_e and R_{in} curves for W(100) and W(110) both cross in the 12 to 15 eV range and with increasing E_p the ratio R_{in}/R_e increases to

a value of ~90 at $E_p = 60$ eV for W(110).

One of the most unusual results of this study is the exceedingly large value of $R_e = 0.75$ as $E_p \rightarrow 0$ as shown in Figure 19 for Ir(111). The Ir(110) results in Figure 20 measured over a larger E_p range also show an increase in R_e at threshold but not nearly as large a value as for Ir(111). From a dynamical point of view, these results suggest the occurrence of a band gap relatively free of surface states approximately 5.79 eV above the Fermi level along the <111> direction of Ir. Both crystals show one additional large peak in R_e at 11.5 and 15 eV for Ir(110) and Ir(111) respectively. While, the variation of R_e with E_p differs sharply for the two crystal faces, the variation of R_{in} with E_p is quite similar. On both crystal faces R_{in} increases monotonically with E_p showing a series of small peaks in the 8 to 30 eV range. No maximum in R_{in} is apparent in this range of E_p as was the case for W(110) and Ni(100). In contrast with the W results the threshold for R_{in} occurs at a higher voltage, i.e., in the 6 to 8 eV range. It is interesting to note that whereas R_t is large for Ir(111) at $E_p = 0$, the value for R_t for Ir(110) is smaller at $E_p = 0$ and increases to a value of 0.7 at 70 eV where it appears to be still increasing with E_p.

The variation of R_e with E_p for Ni(100) is in general agreement with diffraction intensity studies. The peaks in R_e at threshold 15, 28 and 38 eV have been observed elsewhere (49), but with somewhat differing relative magnitudes. The peak near threshold can be ascribed to the first order primary Bragg peak of the 00 band. There is also observed an increase in the elastic peak heights as R_{in} increases in accordance with certain theoretical viewpoints of the electron scattering mechanism (49-51). A large peak normally observed in R_e at 55 eV is missing in the present results. Part of the discrepancy may be due to the presence of a few grain boundaries which de-

veloped near the edge of the Ni(100) crystal prior to obtaining the reflection curves. Although the central portion of the crystal (where the electron beam impinged) appeared monocrystalline (as determined by Laue X-ray), a slight reduction in $\emptyset$ occurred, indicating the possibility of structural effects on the reflection results.

The inelastic reflection threshold for the Ni(100) occurs a few volts above zero and exceeds R_e for $E_p > 16$ eV. A small peak occurs at 18 eV followed by a major maximum at 40 eV. It is clear from the Ni(100) results along with the above mentioned results that inelastic processes become important above 15 to 20 eV and must be considered carefully in theoretical attempts to explain LEED intensity variations with E_p.

The Cu(100) results shown in Figure 22 were obtained for R_t only over a limited range of E_p. Since R_{in} is likely to be small in this energy range $R_t \simeq R_e$. Although not as large as the threshold peak for Ir(111), the threshold peak for Cu(100) is quite large and has been attributed (52) to the well known band gap (53) in the bulk E(k) diagram occurring at the vacuum level. Previous LEED studies of the specular reflectivity I_{oo} from Cu(100) gave a value of $R_e = 0.36$ around $E_p = 1$ eV (52). The results reported here agree closely with the latter results but also show a larger peak at $E_p \simeq 0$ of $R_e = 0.47$. In addition, a very small peak is observed at $E_p = 2.0$ eV. These extremely narrow peaks (less than 0.5 eV) point out the resolving power of this technique near threshold and agree with previous observation that peak widths in R_e below the onset of inelastic reflection are narrower.

VII. SUMMARY

The use of the FERP method to accurately measure true work function of a variety of single crystal surfaces (see Table III) with a minimum of assumptions regarding the nature of the electron emission process has been demonstrated. A combination of the FERP and LEED/Auger should provide a powerful combination of techniques to accurately and conveniently measure bare surface true work functions of conducting surfaces. The occurrence of electron reflection from the collecting surface can generally be tolerated without introducing appreciable error (ca ± 0.02 eV) provided that the work function is obtained from the peak in the TED curve. An unusually large work function of 5.76 eV for Ir(111) was obtained in agreement with an earlier result (31). Other results agreed favorably with previously measured and accepted values of work function.

As shown by Armstrong (47) surface contamination or crystal imperfection can alter the elastic reflectivity versus primary energy curves. This work shows that the FERP technique can yield both elastic and inelastic reflection curves accurately to within a few tenths eV of zero primary energy and thereby can be used as an indicator of surface conditions. Values of R_e and R_{in} for several crystal faces agreed reasonably well with published curves. It is noted that $R_{in} >> R_e$ as $E_p \gtrsim 15$ eV for most crystal faces examined. An unusually large value of R_e was obtained for Ir(111) and Cu(100) at threshold. Whereas the structure in the R_e curves was highly dependent on crystal orientation, the R_{in} curves were generally unaltered by crystal orientation including the threshold values of E_p which were usually 3 to 8 eV.

Finally, it may be anticipated that the FERP technique can be profitably used to examine the combined effect of chemisorption on ϕ, R_e and R_{in}.

BIBLIOGRAPHY

1. Lester, H.H. The determination of the work function when an electron escapes from the surface of a hot body. Philosophical Magazine and Journal of Science 31:197-221. March 1916.

2. Herring, C. and M.H. Nichols. Thermionic emission. Reviews of Modern Physics 21:185-257. April 1949.

3. Lang, N.D. and W. Kohn. Theory of metal surfaces: work function. Physical Review B3:1215-1223, 15 February 1971.

4. Duke, C.B. Electronic structure of clean metallic interfaces. Journal of Vacuum Science and Technology 6:152-166. January/February 1969.

5. Fomenko, V.S. Handbook of thermionic properties. New York, Plenum Press Data Division, 1966. 151p.

6. Rivière, J.C. Work function: measurements and results. Solid State Surface Science 1:179-289. M. Green, Editor. New York, Dekker, 1969.

7. Swanson, L.W. and L.C. Crouser. Total energy distribution of field emitter electrons and single plane work functions for tungsten. Physical Review 163:622-641. 15 November 1967.

8. Sommerfeld, A. Zur elektronentheorie der metalle auf grund der fermischen statistik. I teil: allgemeines, strömungs = aug austrittvorgänge. Zeitschrift für Physik 47:1-32. 7 February 1928.

9. _____, and H. Bethe. Electronentheorie der metalle. Handbuch der physik 24:333-622. Geigrt-Scheel, Editor. Berlin, Springer, 1933.

10. Itskovich, F.I. Effective work functions of different types of electron emission from metals. Soviet Physics JETP 24:202-206. January 1967. Translated from Zhurnal Eksperimental noi i Teoreticheskoi Fiziki (U.S.S.R.) 51:301-308. July 1966.

11. Fowler, R.H. and L.W. Nordheim. Electron emission in intense electric fields. Proceedings of the Royal Society of London A 119:173-181. 1 May 1928.

12. Nordheim, L.W. The effect of the image force on the emission and reflexion of electrons by metals. Proceedings of the Royal Society of London A 121:626-639. 1 December 1928.

13. Swanson, L.W. and L.C. Crouser. Anomalous total-energy distribution for a molybdenum field emitter. Physical Review Letters 19:1179-1181. 13 November 1967.

14. Whitcutt, R.D.B. and B.H. Blott. Band edges at the (111) surface of copper measured by the total energy distribution of field-emitted electrons. Physical Review Letters 23:639-640. 22 September 1969.

15. Shelton, H. Thermionic emission from a planar tantalum crystal. Physical Review 107:1553-1557. 15 September 1957.

16. Young, R.D. and E.W. Müller. Experimental measurement of the total energy distribution of field-emitted electrons. Physical Review 113:115-120. 1 January 1959.

17. van Oostrom, A. Validity of the Fowler-Nordheim model for field electron emission. Philips Research Reports Supplement (Netherlands) No. 1:102p. 1966.

18. Henderson, J.E. and R.E. Badgley. The work required to remove an election. Physical Review 38:590 (abstract only).

19. Dyke, W.P. The work functions of metals from a field current method. Thesis for Doctorate of Philosophy. University of Washington. 1946.

20. Holscher, A.A. A field emission retarding potential method for measuring work functions. Surface Science (Netherlands) 4:89-102. January 1966.

21. Young, R.D. Theoretical total-energy distribution of field-emitted electrons. Physical Review 113:110-114. 1 January 1959.

22. Good, R.H., Jr. and E.W. Müller. Field emission. Handbuch der physik 21:176-231. Berlin, Springer-Verlag, 1956.

23. Swanson, L.W. and A.E. Bell. Recent advances in field electron microscopy of metals. Advances in electronics and electron physics 32:193-309. New York, Academic Press, 1973.

24. Young, R.D. and C.E. Kuyatt. Resolution determination in field emission energy analyzers. Review of Scientific Instruments 39:1477-1480. October 1968.

25. Simpson, J.A. Design of retarding field energy analyzers. Review of Scientific Instruments 32:1283-1293. December 1961.

26. Heil, H. Electron reflection coefficient at zero energy II computer experiments on the reflection of slow electrons in the electrostatic field of surface patches. Physical Review 164: 887-895. 15 December 1967.

27. Everhart, T.E. Simplified analysis of point-cathode electron source. Journal of Applied Physics 38:4944-4957. December 1967.

28. Advanced materials catalog. Orangeburg, New York, Materials Research Corporation, 1969.

29. Steiner, D. and E.P. Gyftopoulos. An equation for the prediction of bare work functions. Report on Twenty-Seventh Annual Conference Physical Electronics. Pp. 160-168. Cambridge, Massachusetts, Massachusetts Institute of Technology, 1967.

30. Protopopov, O.D., E.V. Mikheeva, B.N. Sheinberg and G.N. Shuppe. Emission parameters of tantalum and molybdenum single crystals. Soviet Physics - Solid State 8:909-914. October 1966.

31. Zandberg, E. Ya. and A. Ya. Tontegode. Work function of the iridium (111) face. Soviet Physics - Solid State 12:878-880. October 1970. Translated from Fizika Tuerdogo Tela 12: 1124-1127. April 1970.

32. Protopopov, O.D. and I.V. Strigushchenko. Emission parameters of faces of a niobium single crystal. Soviet Physics - Solid State 10:747-748. September 1968.

33. Bell, A.E., C.J. Bennette, R.W. Strayer and L.W. Swanson. Single crystal clean work functions and behavior of various adsorbates on metal surfaces. NASA-Lewis, Contract Nr. NAS3-11820. McMinnville, Oregon, Field Emission Corporation, 1970.

34. Baker, B.G., B.B. Johnson and G.L.C. Maire. Photoelectric work function measurements on nickel crystals and films. Surface Science (Netherlands) 24:572-586. February 1971.

35. Blevis, E.H. and C.R. Crowell. Temperature dependence of the work function of single-crystal faces of copper. Physical Review 133:A580-A584. 20 January 1964.

36. Smoluchowski, R. Anisotrophy of the electronic work function of metals. Physical Review 60:661-674. 1 November 1941.

37. Feinstein, L.G. and M.S. Macrakis. LEED study of steps and facets on a Re surface. Surface Science (Netherlands) 18: 277-292. December 1969.

38. Delchar, T.A. Oxygen chemisorption on copper single crystals. Surface Science (Netherlands) 27:11-20. August 1971.

39. Smith, J.R. Self-consistent many-electron theory of electron work functions and surface potential characteristics for selected metals. Physical Review 181:522-529. 10 May 1969.

40. Paasch, G., H. Eschrig and W. John. Work function and surface structure of simple metals. Physica Status Solidi (Berlin) 51:283-293. May-June 1972.

41. Smith, J.R. Beyond the local-density approximation: surface properties of (110)W. Physical Review Letters 25:1023-1026. 12 October 1970.

42. Samonov, G.V., Yu. B Paderno and V.S. Fomenko. Thermionic emission characteristics of the transition metals and their compounds. Soviet Physics - Technical Physics 11:1070-1080. February 1967. Translated from Zhurnal Teknicheskei Fiziki 36:1435-1448. August 1966.

43. Dobretsov, L.N. and T.L. Matskevich. Work function of metals. Soviet Physics - Technical Physics 11:1081-1088. February 1967. Translated from Zhurnal Teknicheskoi Fiziki 36:1449-1458. August 1966.

44. Slater, J.C. Quantum theory of molecules and solids Volume 2. New York, McGraw-Hill Book Company, 1965. 563p.

45. Coulson, C.A. Valence. Oxford, Clarendon Press, 1958. 276p.

46. Pauling, L. The nature of the chemical bond. Ithaca, New York, Cornell University Press, 1940. 450p.

47. Armstrong, R.A. The reflection of slow electrons by hydrogen-covered single-crystals of tungsten. Canadian Journal of Physics 44:1753-1764. August 1966.

48. Kahn, I.H., J.P. Hobson and R.A. Armstrong. Reflection and refraction of slow electrons from single crystals of tungsten. Physical Review 129:1513-1523. 15 February 1963.

49. Andersson, S. and B. Kasemo. Low-energy electron diffraction intensities from the clean nickel (001) surface. Surface Science (Netherlands) 25:273-288. April 1971.

50. Capart, G. Dynamical calculations of LEED intensities at clean copper(001) surface. Surface Science (Netherlands) 26:429-453. July 1971.

51. Duke, C.B., J.R. Anderson and C.W. Tucker. The inelastic collision model II. second-order perturbation theory. Surface Science (Netherlands) 19:117-158. January 1970.

52. Andersson, S. Low-energy electron diffraction intensities from the clean copper (001) surface. Surface Science (Netherlands) 18:325-340. December 1969.

53. Burdick, G.A. Energy band of copper. Physical Review 129:138-150. 1 January 1963.

APPENDICES

LENS 1 - .005 I.D.
LENS 2 - .070 I.D.
LENS 3 - .100 I.D.
LENS 4 - .100 I.D.
LENS 5 - .187 I.D.
LENS 6 - .187 I.D.
LENS 7 - .187 I.D.
w/ .080 ϕ .040 INSERTS

EMITTER TIP .030 LONG

TIP - LENS 1 .040 INSIDE, .050 OUTSIDE

1 - 2	.030	SPACE
2 - 3	.035	SPACE
3 - 4	.035	SPACE
4 - 5	.020	SPACE
5 - 6	.020	SPACE
6 - 7	.020	SPACE

MATERIAL - MOLYBDENUM (except those indicated)

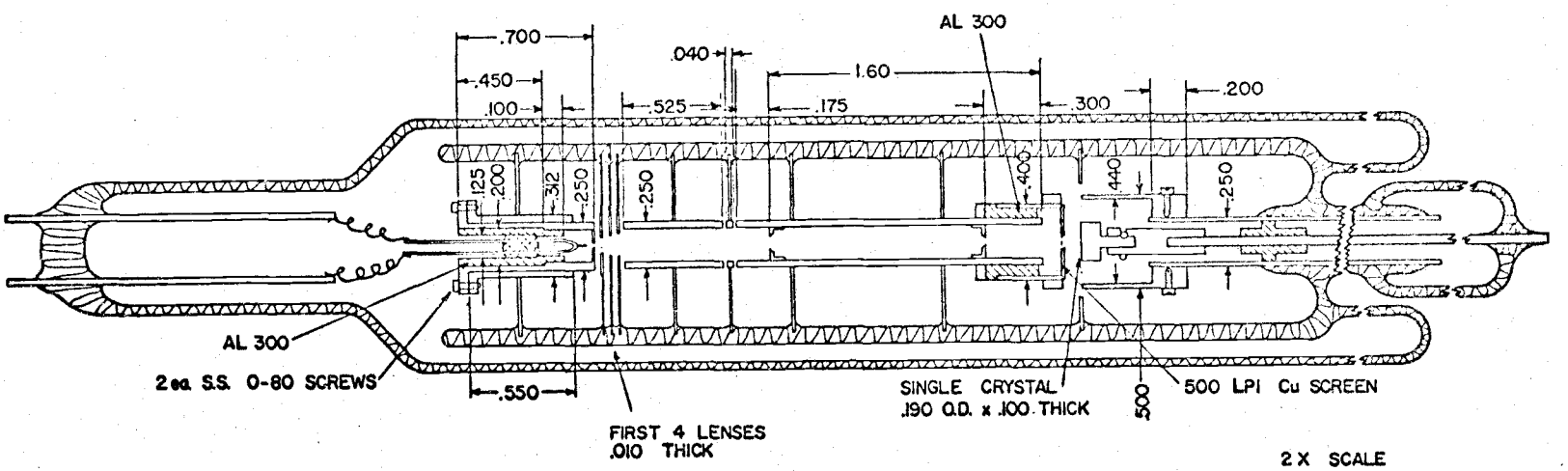

Appendix I: Tube Dimensions

Appendix II: Computer Program

```
C       PHI ,D FROM I(C)-V(C) DATA AND EQ (9)
C       LEAST SQUARES PROGRAM (W.A.M., R.W.S., 1-29-69
C
        DIMENSION C(36), V(36), X(36), DIF(36)
        PRINT 1
        PRINT 2
  100   READ 3, N, TOL, BT, STEP
        PRINT 3,N, TOL, BT, STEP
        SAVE=0.
        CZRO=0.
        CZSAV=0.
        K=1
        L=0
        IF(SENSE SWITCH 3)110,120
  110   PRINT 4
  120   DO 150 I=1,N,1
        READ 5, V(I), C(I)
        IF (CZRO-C(I))190,190,170
  130   CZRO=C(I)+.002
        IF(SENSE SWITCH 3)140,150
  140   PRINT 6, V(I), C(I)
  150   CONTINUE
  160   J=0
        DO 190 I=1,N,1
        IF(CZRO-C(I))190,190,170
  170   SUBA=V(I)
        SUBB=LOG((CZRO-C(I))/CZRO)
        CON=ABS(SUBB)
        IF(CON-BT)190,190,180
  180   J=J+1
        X(J)=SUBA
        Y(J)=SUBB
  190   CONTINUE
  200   SUMX=0.
        SUMY=0.
        SUMXX=0.
        SUMXY=0.
        DO 210 I=1,J,1
        XSUBI=X(I)
        YSUBI=Y(I)
        SUMX=SUMX+XSUBI
        SUMY=SUMY+YSUBI
        SUMXX=SUMXX+XSUBI*XSUBI
  210   SUMXY=SUMXY+XSUBI*YSUBI
        AX=J
        D=SUMX*SUMX-AX*SUMXX
        B=(SUMX*SUMXY-SUMXX*SUMY)/D
        SLOPE=(SUMX*SUMY-AX*SUMXY)/D
        DI=0.
```

```
      DO 220 I=1,J,1
      YSUBI=Y(I)
      DIFFI=B+SLOPE*X(I)-YSUBI
      DI=DI+DIFFI*DIFFI
      DIFSI=DIFFI/YSUBI
  220 DIF(I)=DIFSI
      BDY=DIF(1)
      DO 240 M=1,J,1
      IF(ABS(BDY)-ABS(DIF(M)))230,240,240
  230 BDY=DIF(M)
      LL=M
  240 CONTINUE
      IF(TOL-ABS(BDY))250,260,260
  250 J=J-1
      GO TO 200
  260 W=J
      IF(L-1)270,360,270
  270 IF(SAVE-W)280,280,350
  280 CZSAV=CZRO
      SAVE=J
      IF(SENSE SWITCH 2)290,310
  290 PRINT 7, K, J
      PRINT 8, CZRO, BDY, LL
      IF(SENSE SWITCH 3)300,310
  300 ACCEPT 9, CZRO
      GO TO 340
  310 IF(SENSE SWITCH 1)330,320
  320 CZRO=CZRO-STEP*CZRO
      GO TO 340
  330 CZRO=CZRO+STEP*CZRO
  340 K=K+1
      GO TO 160
  350 L=1
      CZRO=(CZRO+CZSAV)/2.
      GO TO 160
  360 DR=DI*SUMXX/((AX-2.)*D)
      PB=.6745*SQRT(ABS(DR))
      DM=DI*AX/((AX-2.)*D)
      PE=.6745*SQRT(ABS(DM))
      PHI=B/SLOPE
      PEPHI=SQRT((PB/B)*(PB/B)+(PE/SLOPE)*(PE/SLOPE))
      D=1./SLOPE
      PED=PE/SLOPE
      IF(SENSE SWITCH 2)370,400
  370 PRINT 10
      DO 390 I=1,J,1
      IF(SENSE SWITCH 2)380,390
  380 PRINT 11, I, X(I), Y(I), DIF(I)
  390 CONTINUE
  400 PRINT 7, K, J
      PRINT 8, CZRO, BDY, LL
      PRINT 12, PE, PB
```

```
      PRINT 13, SLOPE, B
      PRINT 14, PHI, PEPHI
      PRINT 15, D, PED
      IF(SENSE SWITCH 4)410,420
  410 ACCEPT 9, CZRO
      GO TO 160
  420 GO TO 100
C
    1 FORMAT (36HPHI,D FROM I(C)-V(C) DATA AND EQ (9))
    2 FORMAT (47HLEAST SQUARES PROGRAM (W.A.M.,R.W.S.,
     *     1-29-69))
    3 FORMAT (I4,E7.1,2F7.4,49H
     *                         )
    4 FORMAT (/18HVOLTAGE     CURRENT//)
    5 FORMAT (2F5.2)
    6 FORMAT (F5.2,6X,F5.2)
    7 FORMAT (/8HRUN NO. ,I4,4X,20HNO. OF DATA POINTS =,I4)
    8 FORMAT (8HI ZERO =,F7.3,4X,13HDELTA Y MAX =,2X,E11.4,
     *     2X,10HFOR POINT.,I4)
    9 FORMAT (F6.3)
   10 FORMAT (/8X,2HX                    DELTA Y)
   11 FORMAT (I4,2X,F5.2,2X,F7.4,2X,E11.4)
   12 FORMAT (16HPROB ERR SLOPE =,E11.4,4X,12HPROB ERR B =,
     *     E11.4)
   13 FORMAT (7HSLOPE =,E11.4,4X,3HB =,E11.4)
   14 FORMAT (5HPHI =,F8.4,4X,14HPROB ERR PHI =,E11.4)
   15 FORMAT (3HD =,E11.4,4X,12HPROB ERR D =,E11.4////)
C
C
C     SENSE SWITCH 1     ON  - INCREMENT CZRO UP
C                        OFF - INCREMENT CZRO DOWN
C
C     SENSE SWITCH 2     ON  - TYPE OUT J, K, CZRO, BDY
C                        OFF - DO NOT TYPE OUT
C
C     SENSE SWITCH 3     ON  - ACCEPT NEW CZRO
C                        OFF - INCREMENT CZRO
C
C     SENSE SWITCH 4     ON  - ACCEPT NEW CZRO
C                         OFF - GO TO  NEW HEADER CARD
C                                 AND NEW DATA
C
      END
```